A *Spitzer*–IRS spectroscopic atlas of early-type galaxies in the Revised Shapley–Ames Catalog

R. Rampazzo,[1]★ P. Panuzzo,[2] O. Vega,[3] A. Marino,[4] A. Bressan[5] and M. S. Clemens[1]

[1]*INAF Osservatorio Astronomico di Padova, Vicolo dell'Osservatorio 5, I-35122 Padova, Italy*
[2]*GEPI, Observatoire de Paris, CNRS, Univiversité Paris Diderot, Place Jules Janssen, F-92190 Meudon, France*
[3]*Instituto Nacional de Astrofísica, Optica y Electrónica, Apdos. Postales 51 y 216, CP 72000 Puebla, Pue., Mexico*
[4]*Università degli Studi di Padova, Dipartimento di Fisica e Astronomia 'G. Galilei' Vicolo dell'Osservatorio 3, I-35122 Padova, Italy*
[5] *Scuola Internazionale Superiore di Studi Avanzati (SISSA), via Bonomea, 265 – I-34136 Trieste, Italy*

ABSTRACT

We produce an atlas of homogeneously reduced and calibrated low-resolution IRS spectra of the nuclear regions of nearby early-type galaxies (ETGs, i.e. Es and S0s), in order to build a reference sample in the mid-infrared window. From the *Spitzer* Heritage Archive we extract ETGs in the Revised Shapley–Ames Catalog of Bright Galaxies having an IRS SL and/or LL spectrum. We recover 91 spectra out of 363 galaxies classified as ETGs in the catalogue: 56 E (E0–E6), 8 mixed E/S0+S0/E and 27 S0 (both normal and barred – SB0) plus mixed types SB0/Sa+SB0/SBa. For each galaxy, we provide the fully reduced and calibrated spectrum and the intensity of nebular and molecular emission lines as well as of the polycyclic aromatic hydrocarbons (PAHs) after a template spectrum of a passively evolving ETG has been subtracted. Spectra are classified into five mid-infrared classes, ranging from active galactic nuclei (class-4) and star-forming nuclei (class-3), to transition class-2 (with PAHs) and class-1 (no-PAHs), to passively evolving nuclei (class-0).

A *demographic* study of mid-infrared spectra shows that Es are significantly more passive than S0s: 46^{+11}_{-10} per cent of Es and 20^{+11}_{-7} per cent of S0s have a spectrum of class-0. Emission lines are revealed in 64^{+12}_{-6} per cent of ETGs. The $H_2 S(1)$ line is found with similar rate in Es (34^{+10}_{-8} per cent) and in S0s (51^{+15}_{-12} per cent). PAHs are detected in 47^{+8}_{-7} per cent of ETGs, but only 9^{+4}_{-3} per cent have PAH ratios typical of star-forming galaxies.

Several indicators, such as peculiar morphologies and kinematics, the irregular shape of dust-lanes, and radio and X-ray properties, suggest that mid-infrared spectral classes are associated with phases of accretion/feedback phenomena occurring in the nuclei of ETGs.

Key words: techniques: spectroscopic – galaxies: elliptical and lenticular, cD – galaxies: fundamental parameters – infrared: galaxies.

1 INTRODUCTION

Early-type galaxies (Es and S0s, ETGs hereafter) are the most luminous and massive stellar aggregates in the local Universe and possess a multiphase, sometimes conspicuous, interstellar medium (ISM). The *Spitzer* Space Telescope Heritage Archive (SHA) offers, in the mid-infrared (MIR) window, new tools for use in the endeavour to decipher the evolutionary history of nearby ETGs. Several *Spitzer*–IRS studies have been dedicated to unveiling the MIR spectral characteristics of the nuclear regions of ETGs, leading to the identification of polycyclic aromatic hydrocarbons (PAHs) with

both normal and anomalous inter-band ratios, as well as emission lines from molecular hydrogen (Bregman, Temi & Bregman 2006; Bressan et al. 2006; Kaneda, Onaka & Sakon 2005; Panuzzo et al. 2007; Kaneda et al. 2008; Panuzzo et al. 2011).

Using *Spitzer*–IRS spectra, Bressan et al. (2006) studied the nuclear properties of 20 bright ETGs in the Virgo cluster, identifying a class of *passively evolving* ETGs. Their MIR spectra are characterized by the absence of ionic and molecular emission as well as of PAHs. Only the silicate emission at 10 μm from the circumstellar dust of O-rich asymptotic giant branch (AGB) stars leaves an imprint in these spectra, superimposed on the photospheric stellar continuum generated by red giant stars (Knapp et al. 1989; Athey et al. 2002). The study of Bressan et al. (2006) also shows that ETGs with a passive spectrum are very common in the Virgo cluster (16 out

★E-mail: roberto.rampazzo@oapd.inaf.it

Table 1. The sample of E galaxies.

Galaxy	RSA morph. type	T	D [Mpc]	T88$^{(a-)}$ Group	M_K	r_e [kpc]	σ_c [km s^{-1}]
E							
NGC 636	E1	-4.8 ± 0.5	30	52 -7 7	-23.94	2.8	165
NGC 720	E5	-4.8 ± 0.5	28	52 -9 7	-24.94	4.9	241
NGC 821	E6	-4.8 ± 0.4	24*	52 0 0	-24.00	5.8	200
NGC 1209	E6	-4.5 ± 1.0	36	51-14 14	-24.46	3.2	240
NGC 1275	E pec	-2.2 ± 1.7	72*		-26.16	5.9	259
NGC 1297	E2	-2.5 ± 0.9	29	51 -7 4	-23.36	4.0	115
NGC 1339	E4	-4.3 ± 0.5	20	51 2 1	-22.78	3.9	346
NGC 1374	E0	-4.4 ± 1.1	20	51 -1 1	-23.30	2.4	186
NGC 1379	E0	-4.8 ± 0.5	20	51 -1 1	-23.28	4.0	120
NGC 1395	E2	-4.8 ± 0.5	20	51 -4 4	-24.64	4.7	245
NGC 1399	E1	-4.6 ± 0.5	21	51 -1 1	-25.30	4.1	345
NGC 1404	E2	-4.8 ± 0.5	20	51 -1 1	-24.71	2.3	234
NGC 1407	E0	-4.5 ± 0.7	29	51 -8 4	-25.62	9.9	286
NGC 1426	E4	-4.8 ± 0.5	24	51 -4 4	-23.24	2.9	162
NGC 1427	E5	-4.0 ± 0.9	20	51 -1 1	-23.33	3.0	162
NGC 1453	E2	-4.7 ± 0.7	54		-25.57	6.5	332
NGC 1549	E2	-4.3 ± 0.9	16*	53 -1 1	$-24.24*$	3.5	202
NGC 1700	E3	-4.7 ± 0.9	44		-25.16	3.9	239
NGC 2300	E3	-3.4 ± 1.4	26	42-16 16	-24.51	4.0	261
NGC 2974	E4	-4.2 ± 1.2	21	31-18 18	-25.42	2.5	220
NGC 3193	E2	-4.8 ± 0.5	34	21 -6 6	-24.69	4.0	194
NGC 3258	E1	-4.3 ± 0.9	32	31 -2	-24.25	4.6	271
NGC 3268	E2	-4.3 ± 0.9	35	31 -2	-24.60	6.1	227
NGC 3377	E6	-4.8 ± 0.4	11	15 -1 1	-22.71	1.8	139
NGC 3379	E0	-4.8 ± 0.5	11	15 -1 1	-24.04	1.9	209
NGC 3557	E3	-4.8 ± 0.5	46	31-10 10	-26.13	6.7	265
NGC 3608	E1	-4.8 ± 0.5	23	21 -1 1	-24.80	3.5	192
NGC 3818	E5	-4.6 ± 0.8	36	22 -8 8	-23.95	3.8	191
NGC 3904	E2	-4.7 ± 0.6	28	22 -4 4	-24.61	3.3	205
NGC 3962	E1	-4.8 ± 0.4	35	22 1 1	-25.09	6.0	225
NGC 4261	E3	-4.8 ± 0.4	32	11-24 24	-25.24	5.6	309
NGC 4365	E3	-4.8 ± 0.5	23	11 -5 1	-25.19	5.6	256
NGC 4374	E1	-4.3 ± 1.2	19	11 -1 1	-25.13	4.7	282
NGC 4473	E5	-4.7 ± 0.7	15	11 -1 1	-23.77	1.9	179
NGC 4478	E2	-4.8 ± 0.4	20*	11 -1 1	$-23.15*$	1.3	137
NGC 4486	E0	-4.3 ± 0.6	17	11 -1 1	-25.81	7.8	334
NGC 4564	E6	-4.8 ± 0.5	16	11 -1 1	-23.09	1.5	157
NGC 4589	E2	-4.8 ± 0.4	22	42-13 13	-23.96	1.4	224
NGC 4621	E5	-4.8 ± 0.5	15	11 -1 1	-24.13	2.9	225
NGC 4660	E5	-4.7 ± 0.5	15	11 -1 1	-22.69	0.9	203
NGC 4696	E3	-3.8 ± 0.6	18*	23 -1 1	$-24.13*$	7.4	254
NGC 4697	E6	-4.4 ± 0.8	13	11-11 10	-24.13	4.5	174
NGC 5011	E2	-4.8 ± 0.5	42*	23 0 2	$-24.97*$	4.8	249
NGC 5018	E4	-4.4 ± 1.0	38	11 0 0	-25.23	4.2	209
NGC 5044	E0	-4.8 ± 0.4	31	11-31 31	-24.79	12.4	239
NGC 5077	E3	-4.8 ± 0.4	39	11 0 0	-24.73	4.3	260
NGC 5090	E2	-4.9 ± 0.3	47*	23 0 2	$-25.79*$	14.2	269
NGC 5638	E1	-4.8 ± 0.4	26	41 -3 1	-23.86	3.5	165
NGC 5812	E0	-4.8 ± 0.4	27	41 0 1	-24.22	3.3	200
NGC 5813	E1	-4.8 ± 0.4	32	41 -1 1	-25.15	8.9	239
NGC 5831	E4	-4.8 ± 0.5	27	41 -1 1	-23.75	3.3	164
NGC 7619	E3	-4.7 ± 0.6	53		-25.62	9.5	322
IC 1459	E1	-4.8 ± 0.6	29	61-17 16	-25.53	4.8	311
IC 2006	E1	-4.2 ± 0.9	20	51 -1 1	-23.05	2.8	122
IC 3370	E2 pec	-4.8 ± 0.5	27	23 0 5	-24.32	5.1	202
IC 4296	E0	-4.8 ± 0.4	52		-26.09	10.4	340

$^{(a)}$ The group/cluster identification (Tully 1988, T88) is as follows: 11, Virgo cluster and Southern Extension; 12, Ursa Major Cloud; 13, Ursa Major Southern Spur; 14, Coma–Sculptor Cloud; 15, Leo Spur; 21, Leo Cloud; 22, Crater cloud; 23, Centaurus Cloud; 31, Antlia – Hydra Cloud; 41, Virgo – Libra Cloud; 42, Canes Venatici; 43, Canes Venatici Spur; 44, Draco Cloud; 51, Fornax and Eridanus Cloud; 52, Cetus – Aries Cloud; 53, Dorado Cloud; 61, Telescopium – Grus Cloud; 62, Pavo – Indus Spur; 65, Pegasus Spur.

of 20). The remaining four galaxies include already known 'active' objects such as NGC 4486 (M87) and NGC 4435, the early-type companion in *The Eyes* interacting pair. Buson et al. (2009) showed that the MIR continuum of M87 is the superposition of a passively evolving spectrum and the synchrotron emission from the central active galactic nucleus (AGN). Panuzzo et al. (2007) showed that NGC 4435 has a MIR spectrum typical of star-forming galaxies.

In low-density environments (LDEs), the MIR spectra of ETGs show a large variety of features. In a study of 40 ETGs, located mainly in LDEs, Panuzzo et al. (2011) found that nearly 3/4 of the spectra do not show the passive characteristics found in the Virgo sample of Bressan et al. (2006). Annibali et al. (2010), using optical spectra, had already classified the activity of the ETGs in Panuzzo et al. (2011). Most of their nuclei show characteristics of generic low-ionization nuclear emission-line region galaxies (LIN-ERs), while only a few are either inert/passive or AGN systems. These latter, identified in the optical using nebular line ratios through diagnostic diagrams (see Baldwin, Phillips & Terlevich 1981; Annibali et al. 2010, and reference therein), appear dominated in the MIR by hot dust emission and may show high-ionization emission lines. In the MIR, several optical LINERs show star-forming spectra, similar to NGC 4435, with PAH emission typical of late-type galaxies (Smith et al. 2007). Therefore, MIR spectra provide new clues for an understanding of the mechanisms that power LINERs.

Panuzzo et al. (2011) classified the MIR spectra of ETGs into five spectral classes. The majority of the optical LINERs can be classified into three MIR classes displaying nebular and molecular emission (H_2) without PAHs or with either normal or anomalous PAHs (Bregman et al. 2006; Kaneda et al. 2005, 2007; Vega et al. 2010). Among the spectra with PAHs, the most populated class of MIR spectra (50 per cent) shows anomalous PAH inter-band ratios (7.7-µm/11.3-µm ≤ 2.3). The least populated class shows normal, star-forming, PAH ratios.

Given the short lifetime of PAHs within the ISM of ETGs (Clemens et al. 2010), Panuzzo et al. (2011) proposed that MIR classes may trace the evolutionary phases of a nucleus as the result of an accretion episode. Multiwavelength observations of the Panuzzo et al. (2011) sample support this hypothesis (Annibali et al. 2007; Marino et al. 2011; Rampazzo et al. 2011). Accretion in ETGs may be the result of either secular evolution, driven by bar

Table 2. The sample of E/S0, S0 and SB0 galaxies.

Galaxy	RSA morph. type	T	D [Mpc]	T88[a] Group	M_K	r_e [kpc]	σ_c [km s^{-1}]
E/S0 and S0/E							
NGC 1052	E3/S0	-4.6 ± 0.8	19	52 -1 1	-24.00	3.1	215
NGC 1351	S0$_1$(6)/E6	-3.1 ± 0.6	19	51 -1 1	-22.64	1.9	140
NGC 4472	E1/S0$_1$(1)	-4.8 ± 0.5	17	11 -1 1	-25.73	8.2	294
NGC 4550	E7/S0$_1$(7)	-2.1 ± 0.7	15	11 -1 1	-22.25	1.1	96
NGC 4570	S0$_1$(7)/E7	-2.0 ± 0.7	17	11 -1 1	-23.49	1.5	188
NGC 4636	E0/S0$_1$(6)	-4.8 ± 0.5	15	11 2 1	-24.42	6.4	209
NGC 5353	S0$_1$(7)/E7	-2.1 ± 0.6	30	42 -1 1	-24.74	2.1	286
NGC 6868	E3/S0$_{2/3}$(3)	-4.8 ± 0.6	38*	61 -1 1	-25.58*	6.2	277
S0,SB0,S0/Sa,SB0/Sa							
NGC 584	S0$_1$(3,5)	-4.6 ± 0.9	20	52 -7 7	-24.23	2.4	206
NGC 1366	S0$_1$(8)	-2.3 ± 0.7	17*	51 2 1	-22.14*	0.9	120
NGC 1389	S0$_1$(5)/SB0$_1$	-2.8 ± 0.7	21	51 -1 1	-23.00	1.5	139
NGC 1533	SB0$_2$(2)/SBa	-2.5 ± 0.6	11*	53 -1 1	-22.58*	1.6	174
NGC 1553	S0$_{1/2}$ pec	-2.3 ± 0.6	18*	53 -1 1	-25.00*	5.7	180
NGC 2685	S0$_3$(7) pec	-1.0 ± 0.8	12	13 -4 4	-22.08	1.9	94
NGC 3245	S0$_1$	-2.1 ± 0.5	21	21 -8 8	-23.75	2.7	210
NGC 4036	S0$_3$(8)/Sa	-2.6 ± 0.7	20	12 -5 1	-23.93	3.0	189
NGC 4339	S0$_{1/2}$(0)	-4.7 ± 0.8	16	11 4 1	-22.55	2.5	114
NGC 4371	SB0$_{2/3}$(r)(3)	-1.3 ± 0.6	17	11 -1 1	-23.44	1.9	135
NGC 4377	S0$_1$(3)	-2.6 ± 0.6	18	11 -1 1	-22.43	1.1	144
NGC 4382	S0$_1$(3) pec	-1.3 ± 0.6	18	11 -1 1	-25.13	4.8	178
NGC 4383	S0	-1.0 ± 0.5	22*	11 -1 1	-22.22*	1.2	–
NGC 4435	SB0$_1$(7)	-2.1 ± 0.5	12*	11 -1 1	-23.10*	1.2	157
NGC 4442	SB0$_1$(6)	-1.9 ± 0.4	15	11 -1 1	-23.63	1.8	187
NGC 4474	S0$_1$(8)	-2.0 ± 0.5	15	11 -1 1	-22.27	1.5	88
NGC 4477	SB0$_{1/2}$/SBa	-1.9 ± 0.4	19	11 -1 1	-24.06	3.5	186
NGC 4552	S0$_1$(0)	-4.6 ± 0.9	16	11 -1 1	-24.31	2.3	264
NGC 4649	S0$_1$(2)	-4.6 ± 0.8	16	11 -1 1	-25.35	5.3	335
NGC 5128	S0+S pec	-2.1 ± 0.6	7*	14-15 15	-25.28*		120
NGC 5273	S0/a	-1.9 ± 0.4	17	43 1 1	-22.43	2.5	66
NGC 5631	S0$_3$(2)/Sa	-1.9 ± 0.4	28	42 -7 3	-23.76	2.6	171
NGC 5846	S0$_1$(0)	-4.7 ± 0.7	25	41 -1 1	-25.07	7.6	250
NGC 5898	S0$_{2/3}$(0)	-4.3 ± 0.9	29	41-11 11	-24.31	3.1	220
NGC 7192	S0$_2$(0)	-3.9 ± 0.7	38*	62 -2 1	-24.39*	5.3	257
NGC 7332	S0$_{2/3}$	-1.9 ± 0.5	23	65 -2 1	-23.81	1.6	136
IC 5063	S0$_3$(3) pec/Sa	-1.1 ± 0.5	47*		-24.61*	6.1	160

[a] As in Table 1.

resonances, interaction or minor merger episodes, which may induce nuclear star formation and/or AGN activity. Such activity, fading out with time, leaves traces in emission lines, PAH emission and the underlying continuum, until the nucleus returns to a passive state. MIR spectral classes may also offer snapshots of so-called AGN feedback, namely the interaction between the energy and radiation generated by accretion onto the massive black hole with gas in the host galaxy (Fabian 2012). AGN feedback may arise where

Table 3. *Spitzer*–IRS observations of E galaxies in the Revised Shapley–Ames Catalog of Bright Galaxies.

Galaxy	PI	ID	SL1 [s × Cycle]	SL2 [s × Cycle]	LL2 [s × Cycle]	LL1 [s × Cycle]	Slit [3.6×18 arcsec^2] [kpc × kpc]	Area$_{slit}$/Area$_{r_e/8}$
E								
NGC 636	Bregman	3535	14 × 8	14 × 8	30 × 6	–	0.5 × 2.6	3.5
NGC 720	Bregman	3535	14 × 8	14 × 8	30 × 6	–	0.5 × 2.4	1.0
NGC 821	Bregman	3535	14 × 8	14 × 8	30 × 6	–	0.4 × 2.1	0.5
NGC 1209	Rampazzo	30256	60 × 6	60 × 6	120 × 16	120 × 8	0.6 × 3.1	3.9
NGC 1275	Houck	14	14 × 2	14 × 2	6 × 4	6 × 4	1.3 × 6.3	4.6
NGC 1297	Rampazzo	30256	60 × 19	60 × 19	120 × 14	120 × 8	0.5 × 2.5	1.6
NGC 1339	Bregman	3535	14 × 8	14 × 8	30 × 6	–	0.3 × 1.7	0.8
NGC 1374	Bregman	3535	14 × 8	14 × 8	30 × 6	–	0.3 × 1.7	2.2
NGC 1379	Bregman	3535	14 × 8	14 × 8	30 × 6	–	0.3 × 1.7	0.8
NGC 1395	Kaneda	3619/30483	60 × 2	60 × 2	30 × 2	30 × 2	0.3 × 1.7	0.6
NGC 1399	Bregman	3535	14 × 8	14 × 8	30 × 6	–	0.3 × 1.7	0.8
NGC 1404	Bregman	3535	14 × 8	14 × 8	30 × 6	–	0.4 × 1.8	2.3
NGC 1407	Kaneda	3619/30483	60 × 2	60 × 2	30 × 2	30 × 2	0.5 × 2.5	0.3
NGC 1426	Rampazzo	30256	60 × 12	60 × 12	120 × 14	120 × 8	0.4 × 2.1	2.1
NGC 1427	Bregman	3535	14 × 8	14 × 8	30 × 6	–	0.3 × 1.7	1.4
NGC 1453	Bregman	3535	14 × 8	14 × 8	30 × 6	–	0.9 × 4.7	2.1
NGC 1549	Kaneda	30483	60 × 4	60 × 4	30 × 4	30 × 4	0.3 × 1.4	0.6
NGC 1700	Bregman	3535	14 × 8	14 × 8	30 × 6	–	0.8 × 3.8	3.8
NGC 2300	Bregman	3535	14 × 8	14 × 8	30 × 6	–	0.4 × 2.3	1.3
NGC 2974	Kaneda	3619/30483	60 × 2	60 × 2	30 × 3	30 × 3	0.4 × 1.8	2.2
NGC 3193	Appleton	50764	14 × 4	14 × 3	30 × 2	30 × 2	0.6 × 3.0	2.2
NGC 3258	Rampazzo	30256	60 × 8	60 × 8	120 × 14	120 × 8	0.6 × 2.8	1.4
NGC 3268	Rampazzo	30256	60 × 9	60 × 9	120 × 14	120 × 8	0.6 × 3.0	1.0
NGC 3377	Bregman	3535	14 × 8	14 × 8	30 × 6	–	0.2 × 1.0	1.1
NGC 3379	Bregman	3535	14 × 8	14 × 8	30 × 6	–	0.2 × 1.0	1.1
NGC 3557	Kaneda	30483	60 × 3	60 × 3	30 × 3	30 × 3	0.8 × 4.0	1.5
NGC 3608	Bregman	3535	14 × 8	14 × 8	30 × 6	–	0.4 × 2.0	1.3
NGC 3818	Rampazzo	30256	60 × 19	60 × 19	120 × 14	120 × 8	0.6 × 3.1	2.7
NGC 3904	Kaneda	30483	60 × 3	60 × 3	30 × 4	30 × 4	0.5 × 2.4	2.2
NGC 3962	Kaneda	3619/30483	60 × 2	60 × 2	30 × 3	30 × 3	0.6 × 3.0	1.1
NGC 4261	Antonucci	20525	240 × 2	240 × 3	120 × 3	120 × 2	0.6 × 2.8	1.0
NGC 4365	Bressan	3419	60 × 3	60 × 3	120 × 3	–	0.4 × 2.0	0.5
NGC 4374	Rieke	82	60 × 4	60 × 4	120 × 4	120 × 4	0.3 × 1.7	0.5
NGC 4473	Bressan	3419	60 × 3	60 × 3	120 × 3	–	0.3 × 1.3	1.9
NGC 4478	Bregman	3535	14 × 8	14 × 8	30 × 6	–	0.3 × 1.7	7.3
NGC 4486	Bressan	3419	60 × 3	60 × 3	120 × 3	–	0.3 × 1.5	0.1
NGC 4564	Bressan	3419	60 × 4	60 × 4	120 × 6	–	0.3 × 1.4	3.3
NGC 4589	Kaneda	3619/30483	60 × 2	60 × 2	30 × 2	30 × 2	0.4 × 1.9	7.9
NGC 4621	Bressan	3419	60 × 3	60 × 3	120 × 3	–	0.3 × 1.3	0.8
NGC 4660	Bressan	3419	60 × 3	60 × 3	120 × 5	–	0.3 × 1.3	8.8
NGC 4696	Kaneda	3619/30483	60 × 2	60 × 2	30 × 3	30 × 3	0.3 × 1.6	0.2
NGC 4697	Bregman	3535	14 × 8	14 × 8	30 × 6	–	0.2 × 1.1	0.3
NGC 5011	Rampazzo	30256	60 × 6	60 × 6	120 × 12	120 × 8	0.7 × 3.7	2.3
NGC 5018	Kaneda	30483	60 × 4	60 × 4	30 × 3	30 × 3	0.7 × 3.3	2.5
NGC 5044	Rampazzo	30256	19	19	14	8	0.5 × 2.7	0.2
NGC 5077	Rampazzo	30256	60 × 12	60 × 12	120 × 14	120 × 8	0.7 × 3.4	2.5
NGC 5090	Kaneda	30483	60 × 4	60 × 4	30 × 3	30 × 3	0.8 × 4.1	0.3
NGC 5638	Bregman	3535	14 × 8	14 × 8	30 × 6	–	0.4 × 2.3	1.7
NGC 5812	Bregman	3535	60 × 6	60 × 6	120 × 12	120 × 8	0.5 × 2.4	2.0
NGC 5813	Bregman	3535	14 × 8	14 × 8	30 × 6	–	0.6 × 2.8	0.4
NGC 5831	Bregman	3535	14 × 8	14 × 8	30 × 6	–	0.5 × 2.4	2.0
NGC 7619	Bregman	3535	14 × 8	14 × 8	30 × 6	–	0.9 × 4.6	1.0
IC 1459	Kaneda	30483	60 × 3	60 × 3	30 × 2	30 × 2	0.5 × 2.5	1.1
IC 2006	Bregman	3535	14 × 8	14 × 8	30 × 6	–	0.3 × 1.7	1.6
IC 3370	Kaneda	3619/30483	60 × 2	60 × 2	30 × 3	30 × 3	0.5 × 2.4	0.9
IC 4296	Antonucci	20525	240 × 2	240 × 2	120 × 3	120 × 3	0.9 × 4.5	0.8

the intense flux of photons and particles, produced by the AGN, strips the interstellar gas, halting both star formation and accretion onto the AGN itself.

Testing these hypotheses motivated us to search the *Spitzer* Archive for high-signal-to-nose ratio, low-resolution IRS spectra in the quest for a larger sample of well-studied, nearby ETGs. To this end we used the Revised Shapley–Ames Catalog of Bright Galaxies (RSA hereafter) (Sandage & Tammann 1987) as our starting point. RSA classifies 363 nearby galaxies as ETGs; although it is not a complete catalogue (Sandage & Tammann 1987), it is certainly representative of bright nearby galaxies. We found 91 ETGs with *Spitzer*–IRS spectra. This paper organizes this material, homogeneously reduced and calibrated. The present atlas is intended to be a window onto the MIR properties of the nuclear regions of nearby ETGs and to contribute to the understanding of their evolution. A local reference sample, made of well-studied ETGs, may be used to make comparisons with numerous distant sources discovered by *Spitzer*–IRS (e.g. Sargsyan et al. 2011).

The paper is organized as follows. In Section 2 we present the characteristics of the *Spitzer*–IRS sample. Section 3 provides information about observations and the strategy for spectrum extraction and calibration. ETG spectra are analysed in Section 4, where we provide a measure of atomic and molecular emission lines and PAH intensities. We finally classify spectra into the MIR spectral classes devised by Panuzzo et al. (2011). In Section 5 we perform a *demographic* study of the MIR spectral classes as a function of morphological type, the galaxy environment, as well as the X-ray, CO and radio properties of the galaxies derived from the literature. In Section 6 we investigate MIR classes in the light of morphological and kinematical peculiarities widely used to infer the recent evolutionary history of ETGs.

2 THE SAMPLE

We cross-match RSA with the *Spitzer* Heritage Archive, including IRS spectra either with just SL segments or both SL and LL segments, as our priority is to characterize spectral features and obtain the MIR classification of the spectra as in Panuzzo et al. (2011). In Tables 1 and 2 we list the resulting sample of 91 ETGs, and in Tables 3 and 4 we give the basic observational parameters. Although by no means complete, this atlas doubles the Panuzzo et al. (2011) sample, the largest study to date.

Table 4. *Spitzer*–IRS observations of E/S0s and S0s in the Revised Shapley–Ames Catalog of Bright Galaxies.

Galaxy	PI	ID	SL1 [s × Cycle]	SL2 [s × Cycle]	LL2 [s × Cycle]	LL1 [s × Cycle]	Slit [3.6 × 18arcmin²] [kpc × kpc]	$Area_{slit}/Area_{r_e/8}$
E/S0 and S0/E								
NGC 1052	Kaneda	30483	60 × 2	60 × 2	30 × 2	30 × 2	0.3 × 1.7	1.2
NGC 1351	Bregman	3535	14 × 8	14 × 8	30 × 6	–	0.3 × 1.7	3.2
NGC 4472	Bregman	3535	14 × 8	14 × 8	30 × 6	–	0.3 × 1.5	0.1
NGC 4550	Bressan	3419	60 × 20	60 × 20	120 × 14	–	0.3 × 1.3	5.8
NGC 4570	Bressan	3419	60 × 3	60 × 3	120 × 5	–	0.3 × 1.5	4.2
NGC 4636	Bressan	3419	60 × 3	60 × 3	120 × 5	–	0.2 × 1.3	0.2
NGC 5353	Appleton	50764	60 × 1	60 × 1	30 × 2	30 × 2	0.5 × 2.6	6.1
NGC 6868	Rampazzo	30256	60 × 6	60 × 6	120 × 13	120 × 8	0.7 × 3.3	1.2
S0,SB0,S0/Sa,SB0/Sa								
NGC 584	Bregman	3535	14 × 8	14 × 8	30 × 6	–	0.3 × 1.7	2.1
NGC 1366	Rampazzo	30256	60 × 11	60 × 11	120 × 14	120 × 8	0.3 × 1.5	11.7
NGC 1389	Rampazzo	30256	60 × 9	60 × 9	120 × 14	120 × 8	0.4 × 1.8	5.8
NGC 1533	Rampazzo	30256	60 × 3	60 × 3	120 × 5	120 × 3	0.2 × 1.0	1.5
NGC 1553	Rampazzo	30256	60 × 3	60 × 3	120 × 3	120 × 3	0.3 × 1.6	0.3
NGC 2685	Rieke	40936	14 × 6	14 × 6	14 × 6	14 × 6	0.2 × 1.0	1.3
NGC 3245	Sturm	3237	14 × 2	14 × 2	–	–	0.3 × 1.8	1.8
NGC 4036	Sturm	3237	14 × 2	14 × 2	–	–	0.3 × 1.7	1.4
NGC 4339	Bressan	3419	60 × 20	60 × 20	120 × 14	–	0.3 × 1.4	1.3
NGC 4371	Bressan	3419	60 × 9	60 × 9	120 × 10	–	0.3 × 1.5	2.4
NGC 4377	Bressan	3419	60 × 12	60 × 12	120 × 8	–	0.3 × 1.6	7.7
NGC 4382	Bressan	3419	60 × 3	60 × 3	120 × 3	–	0.3 × 1.6	0.4
NGC 4383	Weedman	50834	60 × 2	60 × 2	120 × 1	120 × 1	0.4 × 1.9	10.5
NGC 4435	Bressan	3419	60 × 3	60 × 3	120 × 5	–	0.2 × 1.0	3.1
NGC 4442	Bressan	3419	60 × 3	60 × 3	120 × 3	–	0.3 × 1.3	2.2
NGC 4474	Bressan	3419	60 × 20	60 × 20	120 × 24	–	0.3 × 1.3	3.1
NGC 4477	Riecke	40936	14 × 6	14 × 6	14 × 6	14 × 6	0.3 × 1.7	0.9
NGC 4552	Bregman	3535	14 × 8	14 × 8	30 × 6	–	0.3 × 1.4	1.5
NGC 4649	Bregman	3535	14 × 8	14 × 8	30 × 6	–	0.3 × 1.4	0.3
NGC 5128	Houck/Lacy	14	6 × 4/6 × 4	6 × 4/6 × 4	6 × 4	6 × 4	0.1 × 0.6	
NGC 5273	Riecke	40936	6 × 2		6 × 2	6 × 2	0.3 × 1.5	1.4
NGC 5631	Riecke	40936	14 × 6	14 × 6	14 × 6	14 × 6	0.5 × 2.4	3.7
NGC 5846	Bregman	3535	14 × 8	14 × 8	30 × 6	–	0.4 × 2.2	0.3
NGC 5898	Rampazzo	30256	60 × 11	60 × 11	120 × 14	120 × 8	0.5 × 2.5	2.7
NGC 7192	Rampazzo	30256	60 × 12	60 × 12	120 × 14	120 × 8	0.7 × 3.3	1.6
NGC 7332	Rampazzo	30256	60 × 7	60 × 7	120 × 14	120 × 8	0.4 × 2.0	6.1
IC 5063	Gorjan	30572	14 × 2	14 × 2	30 × 1	30 × 1	0.8 × 4.1	1.8

ETGs are divided according to their RSA morphological classification (column 2) into Es and S0s. In the S0 family we include both bona fide S0s, in their normal and barred forms, and the 'mixed' subclasses E/S0 and S0/E. Tables 1 and 2 also report the morphological type code, T (column 3), provided in Hypercat. The sample of Es is composed of 56 galaxies: the subclasses from E0 to E6 are all populated. The sample of S0s consists of 35 galaxies of several subtypes, including mixed cases, namely E/S0, S0/Sa and SB0/Sa. In all cases the morphological type code, T, is ≤ 0, as expected for ETGs. Most of the E galaxies have $T \leq -3$. Remarkable exceptions are NGC 1297 ($T = -2.5 \pm 0.9$) and NGC 1275 ($T = -2.2 \pm 1.7$), classified as E-S0 and S0, respectively, in Hypercat. S0s in RSA span all the $T < 0$ range, consistent with their mixed nature. About 1/3 of the class E/S0 + S0 (see Table 2) are considered truly Es ($T \leq -3$) in Hypercat.

The redshift-independent distances, D (column 4), and the absolute K magnitudes, M_K (column 6), are from the Extragalactic Distance Database (Tully et al. 2009), and the effective radius, r_e (column 7), is from RC3 (de Vaucouleurs et al. 1991). For galaxies labelled with an asterisk we use a Hubble constant of 73 km s^{-1} Mpc^{-1} and the heliocentric velocity, V_{hel}, from the NASA/IPAC Extragalactic Database (NED). Most of the galaxies in the sample have a heliocentric systemic velocity lower than 3500 km s^{-1}. Only NGC 1275, 1453, 1700, 7619 and IC 4296 exceed this limit. In the global sample, distances of the galaxies are less than 72 Mpc. For each galaxy we report the cluster/group association to which the galaxy should be gravitationally bound (see column 5 and the footnote for Table 1). These data are provided in the T3000 catalogue (Tully et al. 2009). Es and S0s are located in different environments. Our sample includes 31 cluster members, 21 located in the denser regions of the Virgo cluster (T88 group 11 -1 1, 11 $+2$ $+1$) and 8 of the Fornax cluster (T88 group 51 -1 1). According to Tully (1988), the environmental density associated with cluster members is $\rho \geq 1.33$ (gal Mpc^{-3}). Two additional galaxies, NGC 1275 (Perseus cluster) and NGC 7619 (Pegasus I cluster), too distant to be found in Tully's catalogue, have been included in the present cluster sample. The remaining 60 ETGs are located in LDEs and have $\rho \leq 0.97$ (gal Mpc^{-3}).

Our sample of Es and S0s presents fundamental characteristics noticed in different samples. In Tables 1 and 2 we report
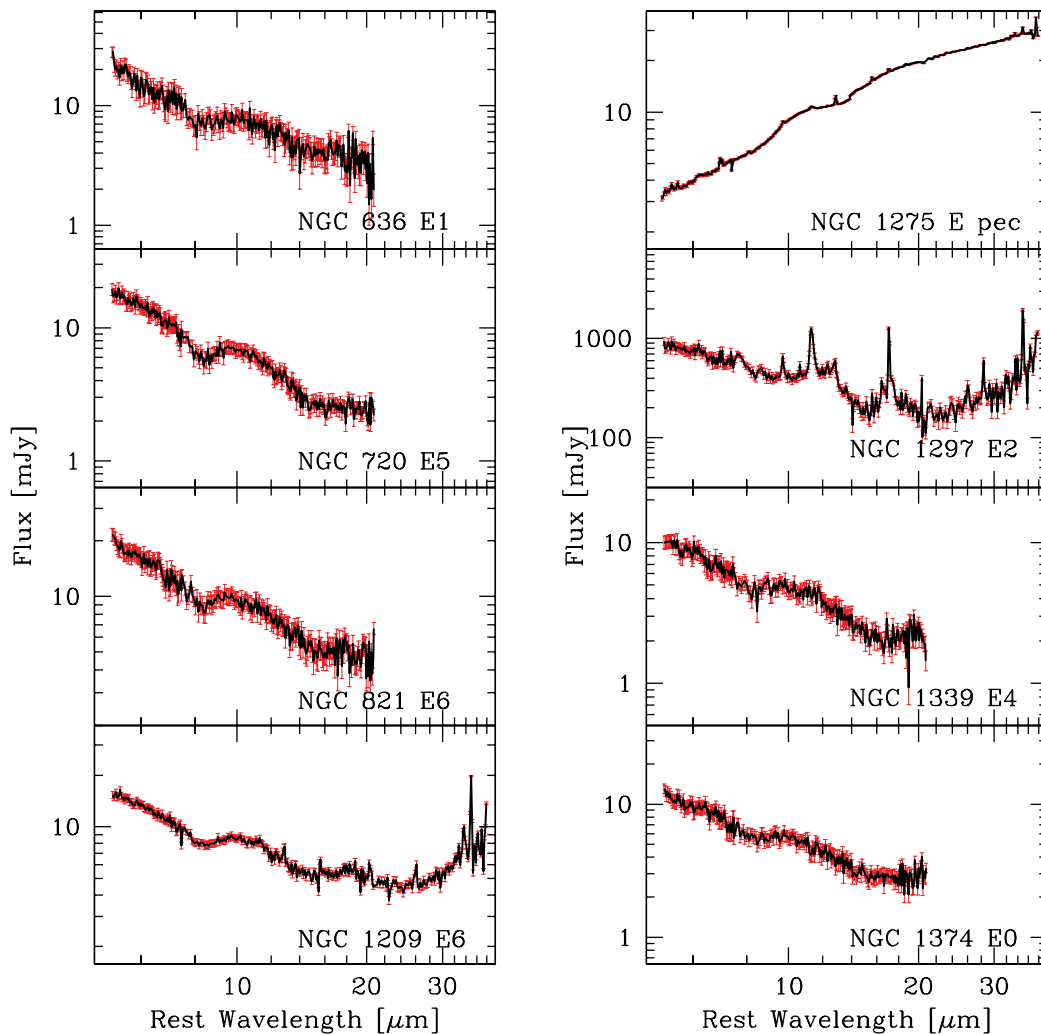
Figure 1. Spectra of Es flux versus rest wavelength as obtained from *Spitzer*–IRS low-resolution modules. Bars represent the 1σ error. The LL modules have been scaled to match the SL fluxes. For IC 3370 (see Kaneda et al. 2008), the SL observations miss the centre of the galaxy by 10 arcsec, which caused a significant reduction in the signal-to-noise ratio of the SL spectrum. In the case of NGC 4472, the LL2 module has been arbitrarily scaled. The spectrum of NGC 4339 shows absorption features at 9 and 13 µm, which are data-reduction artefacts resulting from a bright source falling in the peak-up blue field of view during the observation.

the M_K (column 6), a proxy of the stellar mass, and the central velocity dispersion (column 8), σ_c (from Hypercat), a proxy of the total galaxy mass (Clemens et al. 2006, 2009). We applied a Mann–Whitney U-test (Wall 1977) to both the M_{K_T} and σ_c distributions of Es and of S0s to compare the properties of the two samples. We verified the null hypothesis that the two samples result from the same parent population can be rejected at the 99 per cent confidence level. The medians of the M_{K_T} and σ_c distributions for Es are larger than those for S0s, suggesting that Es are less dominated by dark matter than S0s of a similar total mass. Shankahr, Salucci & Danese (2004, their fig. 1) noticed that the different dominance of dark matter in Es with respect to S0s suggests that the two morphological families had different evolution mechanisms.

3 OBSERVATIONS AND DATA REDUCTION

The details of the *Spitzer*–IRS observations for each galaxy are provided in Tables 3 and 4 for Es and S0s, respectively. In column 8 we provide the slit aperture in kiloparsecs. In column 9, the ratio between the area covered by the slit and the circular aperture of radius $r_e/8$ is given. Although we used a fixed aperture for the

extraction of the spectra, the slit covers the central portions of the ETGs, with a size, on average, of about $2–3 \times \pi(r_e/8)^2$ (1.9 ± 1.8 for Es and 2.9 ± 2.8 for S0s). We refer to this portion as the 'nuclear' part of the galaxy throughout the paper.

Observations were performed in Standard Staring mode with low-resolution ($R \sim 64–128$) modules SL1 (7.4–14.5 µm), SL2 (5–8.7 µm), LL2 (14.1–21.3 µm) and LL1 (19.5–38 µm). Observations do not include, in general, all IRS modules.

The data reduction procedure is fully described in Panuzzo et al. (2011). In the following we briefly recall the main steps of the reduction. After the removal of bad pixels from the co-added images, the sky background was removed by subtracting co-added images taken with the source placed in different orders at the same nod position. Offset exposures, if available, were used to measure the sky background without contamination from the target galaxy itself. For those galaxies for which only the LL2 module was used, the background subtraction was performed by subtracting co-added images taken with the source at different nod positions.

In order to derive calibrated spectral energy distributions, we took into account that the galaxies are extended, compared with the IRS point spread function (PSF). Because the IRS spectra are calibrated on point-sources, we devised an ad hoc procedure to correct for
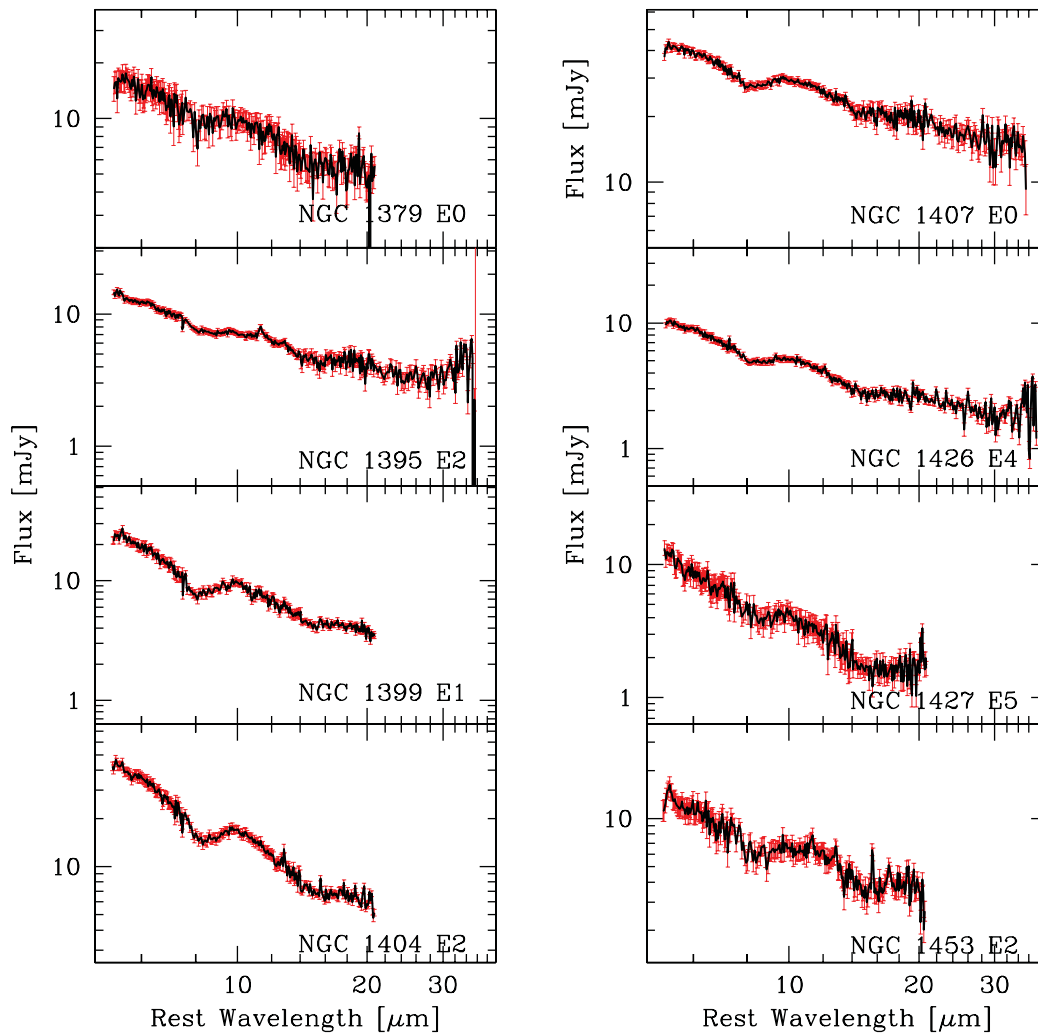
Figure 1 – *continued*

the effects of the variation with wavelength of the IRS PSF. We simulated the effect of convolving an intrinsic surface brightness profile (a modified King's law, Elson, Fall & Freeman 1987) with the instrumental PSF, and of the extraction in a fixed width of 3.6 arcsec. This provides a correction factor to be applied to the extracted spectrum as a function of the wavelength and the profile parameters. By fitting the observed profiles with the simulated ones, we can reconstruct the intrinsic profiles and correct the extracted spectra to correspond to the intrinsic SED. This procedure also has the advantage of determining whether a particular feature is spatially extended or not.

This procedure was applied to SL modules but not to LL modules, for which the PSF is too large to determine the intrinsic surface brightness profile. For this reason, the spectra in the LL range were extracted as if the sources were point-like and then manually scaled to match the SL segment. This is equivalent to assuming that the light distribution at LL wavelengths is the same as that at the end of the SL segment. Note that for those sources that are fully dominated by the nucleus (i.e. AGN-dominated, such as NGC 1275) there is no need to rescale the LL spectra.

The rest-frame, flux-calibrated IRS spectra of the sample galaxies are shown in Fig. 1.

4 SPECTRAL PROPERTIES OF THE ATLAS

The present atlas aims to build, from homogeneously reduced *Spitzer*–IRS spectra, a data set of emission lines and PAH intensities, as well as to divide nearby ETG nuclei into MIR physical classes as in Panuzzo et al. (2011).

4.1 Analysis of MIR spectra

To analyse spectra we adopted a model of the MIR emission that takes into account the following components: (i) the underlying stellar continuum due to the old population characteristic of a passively evolving ETG, which includes the contribution of the dusty AGB stars that dominate the emission at wavelengths $\leq 6\,\mu m$ (Bressan et al. 2006); (ii) a featureless thermal continuum representing a putative dust contribution at longer wavelengths; (iii) the emission from molecular and atomic lines; and (iv) the PAH features. The best fit of each spectrum is obtained using the Levenberg–Marquardt algorithm.

The model is fully described in Vega et al. (2010) and Panuzzo et al. (2011) and is similar to that used by Smith et al. (2007). The main difference consists in the selection of the underlying stellar
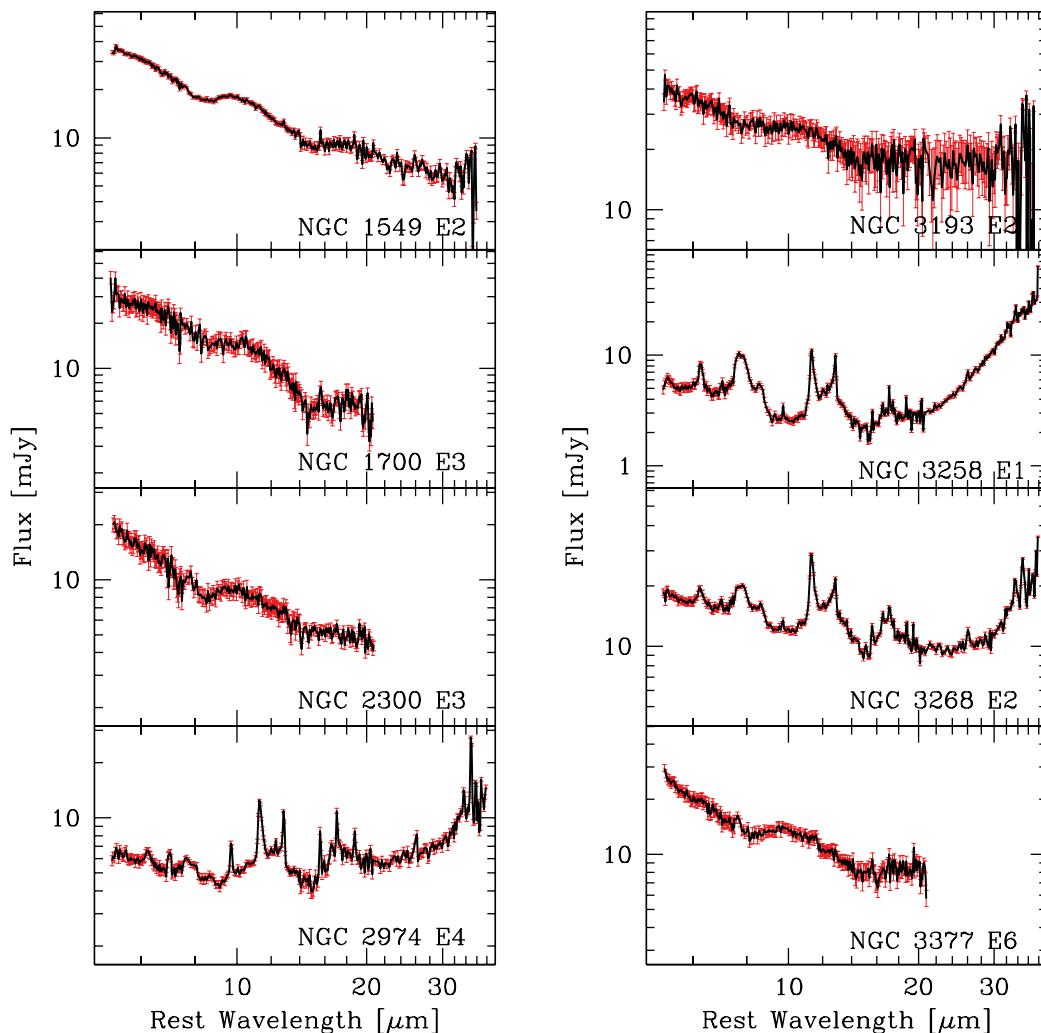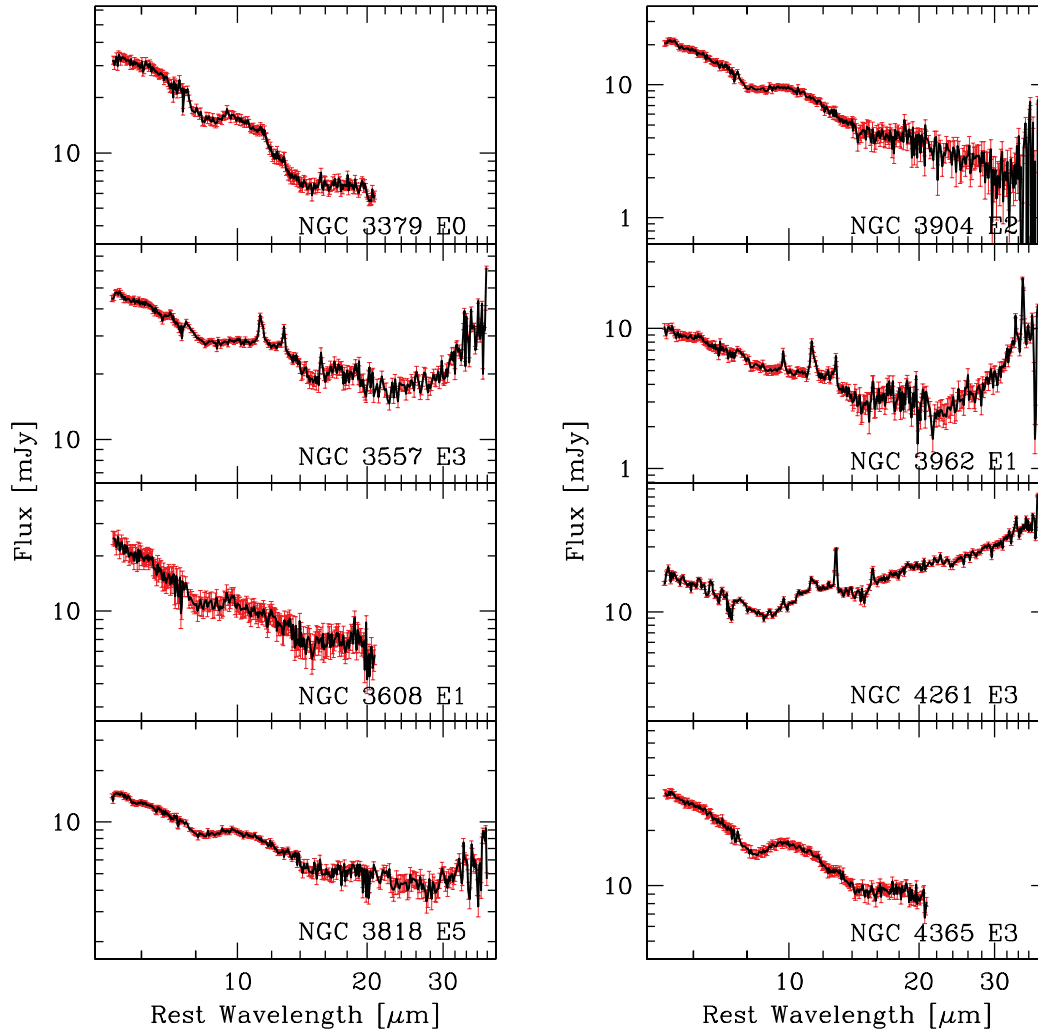
Figure 1 – *continued*

Figure 1 – *continued*

continuum component. The stellar component is described by Smith et al. (2007) as the emission of a blackbody at 5000 K. This approximation, suitable for the analysis of star-forming galaxies, where the hot dust and PAH features dominate the MIR emission, is not adequate for ETGs. In these galaxies, the underlying stellar component usually dominates the MIR continuum at shorter wavelengths, and the MIR emission is characterized by a dip at 8 μm, probably due to photospheric SiO absorption bands (Verhoelst et al. 2009), and by a bump at ∼10 μm from the silicate emission from the dusty circumstellar envelopes of O-rich AGB stars (e.g. Bressan et al. 1998; Bressan et al. 2006). We therefore adopt a semi-empirical, high signal-to-noise ratio template derived from the analysis of passive ETGs in Panuzzo et al. (2011) to describe the stellar continuum. The template is built by averaging the NIR (*J-H-K* 2MASS) data, within the central 5-arcsec radius, and the 5–40 μm *Spitzer*–IRS spectra of three passively evolving ETGs, namely NGC 1389, 1426 and 3818. The subtraction of the underlying stellar continuum is performed by assuming that the NIR fluxes are completely attributable to the stellar component. Thus, we normalize our stellar continuum template to the observed flux in the *H* band, and calculate the contribution of the stellar continuum to the MIR spectra. Fig. 2 provides some examples of the MIR continuum in different types of spectra, and Fig. 3 shows some examples of the fitting procedure (see also next section).

Measurements of PAH features and of the nebular and molecular emission lines are collected in the Appendix, Tables A1 and A2, respectively.

4.2 MIR spectral classes

Panuzzo et al. (2011) subdivided low-resolution *Spitzer*–IRS spectra into five classes, from class-0 to class-4. Class-0 defines passively evolving nuclei. Classes 1 to 4 aim to categorize spectra related to different powering mechanisms active in the nuclear regions. The classification scheme is based on (i) the detection of emission (atomic and/or molecular) lines and PAH features, (ii) the values of the PAH inter-band ratios, and (iii) the presence of an excess in the MIR continuum over the underlying old stellar population.

We briefly summarize below the classification criteria of Panuzzo et al. (2011). Class-0 spectra show neither ionic, molecular nor PAH emission lines superimposed on the photospheric stellar continuum generated by red giant stars. Only the silicate features at ∼10 μm (Bressan et al. 2006) and at 18 μm (Panuzzo et al. 2011), arising from the circumstellar dust of O-rich AGB stars (Bressan, Granato & Silva 1998), are present in these spectra.

Class-1 spectra show either nebular or molecular emission lines but no PAHs. Ionic, in particular [Ne II] 12.8 μm, [Ne III] 15.5 μm, [S III] 18.7 μm, 33.5 μm and molecular H_2 0-0 rotational emission

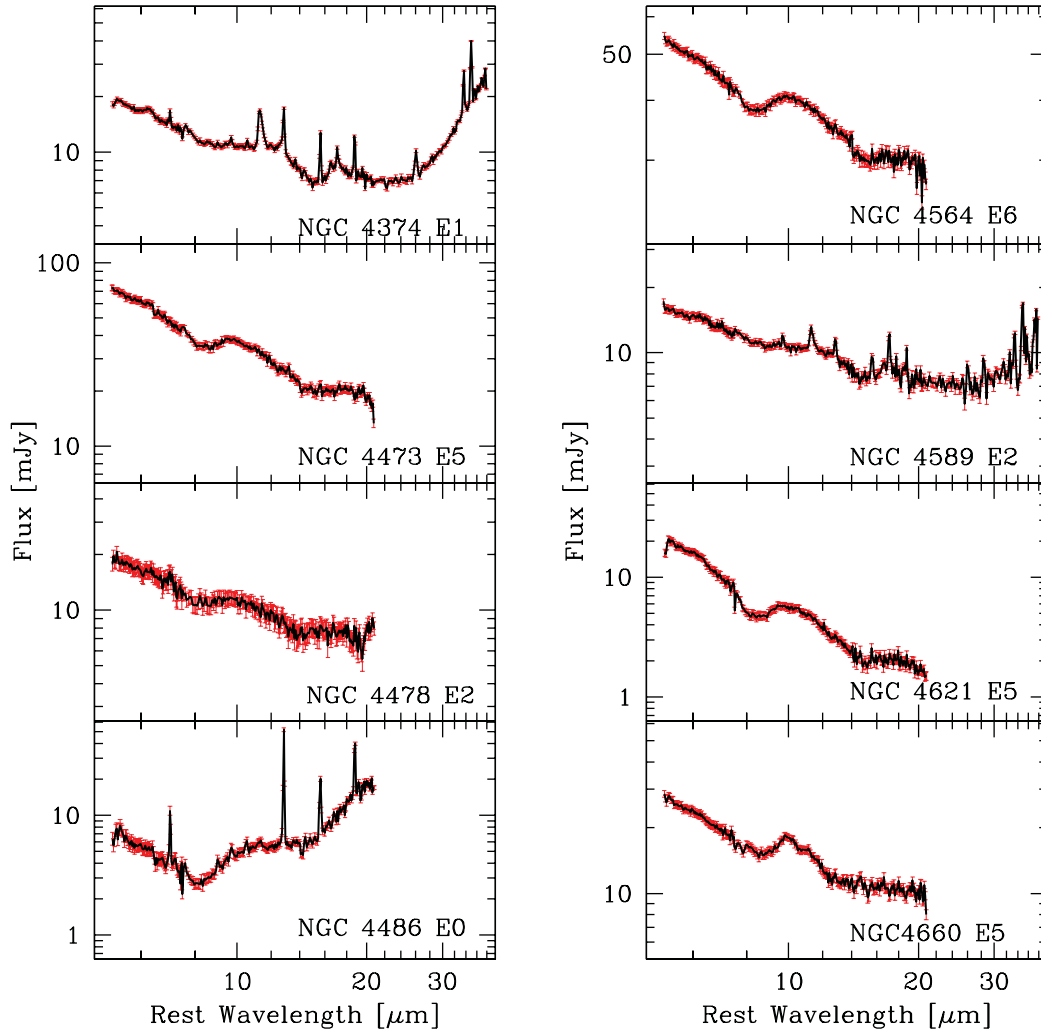**Figure 1** – *continued*

lines (S(n)) are detected. The continuum of this class is similar to that of passive class-0 ETGs, at least up to 25 μm, showing, in some cases, dust emission at longer wavelengths.

All other classes show PAH complexes plus gas, ionic and molecular, emission lines. These latter include forbidden nebular emission lines of several elements such as Ar, Fe, N, O, S and Si. PAH emission features are typically detected at 6.2, 7.7, 8.6, 11.3, 12.7 and 17 μm (Bregman et al. 2006; Bressan et al. 2006; Kaneda et al. 2005; Panuzzo et al. 2007; Kaneda et al. 2008; Panuzzo et al. 2011).

Classes 2 and 3 are distinguished through their different PAH inter-band ratios. Class-2 spectra have an anomalous PAH inter-band ratio, 7.7-μm/11.3-μm ≤2.3. We set this value as the lower limit for class-3 because, in their fig. 14, Smith et al. (2007) show that some H ii-dominated sources and star-forming galaxies may reach this low PAH inter-band ratio. Class-3 spectra are dominated by the 7.7-, 11.3-, 12.7- and 17-μm PAH complexes and have normal PAH inter-band ratios typical of star-forming galaxies (Smith et al. 2007).

Finally, spectra dominated by a hot dust continuum are collected in the MIR class-4 (see discussion below). Emission lines with high ionization such as [S iv] and [Ne v] and PAH features may sometimes be visible.

Fig. 2 illustrates the variation of the continuum in the various MIR classes. The presence of emission lines starts from class-1, and the importance of PAH features increases from class-2 to class-3. Detailed fits of line and PAH emission features are shown in Fig. 3 for NGC 4477 (class-2, top panel), NGC 5018 (class-3, mid panel) and NGC 1052 (class-4, bottom panel).

The contribution of the old stellar population to the MIR continuum decreases from class-0 to class-3, becoming almost negligible in class-4. Fig. 4 shows ETGs in the colour–colour 2MASS *J*-band/6-μm versus 6-μm/15-μm plane, which considers the MIR excess over the underlying old stellar population owing to the hot dust. ETG nuclei of classes 3 and 4 are clearly separated from more quiescent ones (classes 0 and 1) and partly from class-2 nuclei. More quiescent ETGs are all located within a region (the rectangle in the top panel of Fig. 4) delimited by old single stellar population (SSP) models (age: 10–14.5 Gyr and metallicity 0.004 ≤ Z ≤ 0.05, i.e. ~1/4 to 3Z$_\odot$; Bressan et al. 1998). The 6-μm/15-μm value of NGC 4261 sets our empirical upper limit of class-4 ETGs. This value of the MIR excess is comparable, within errors, to NGC 4486, for which Buson et al. (2009) show that the MIR continuum is just the superposition of a passively evolving spectrum and synchrotron emission from the central AGN.
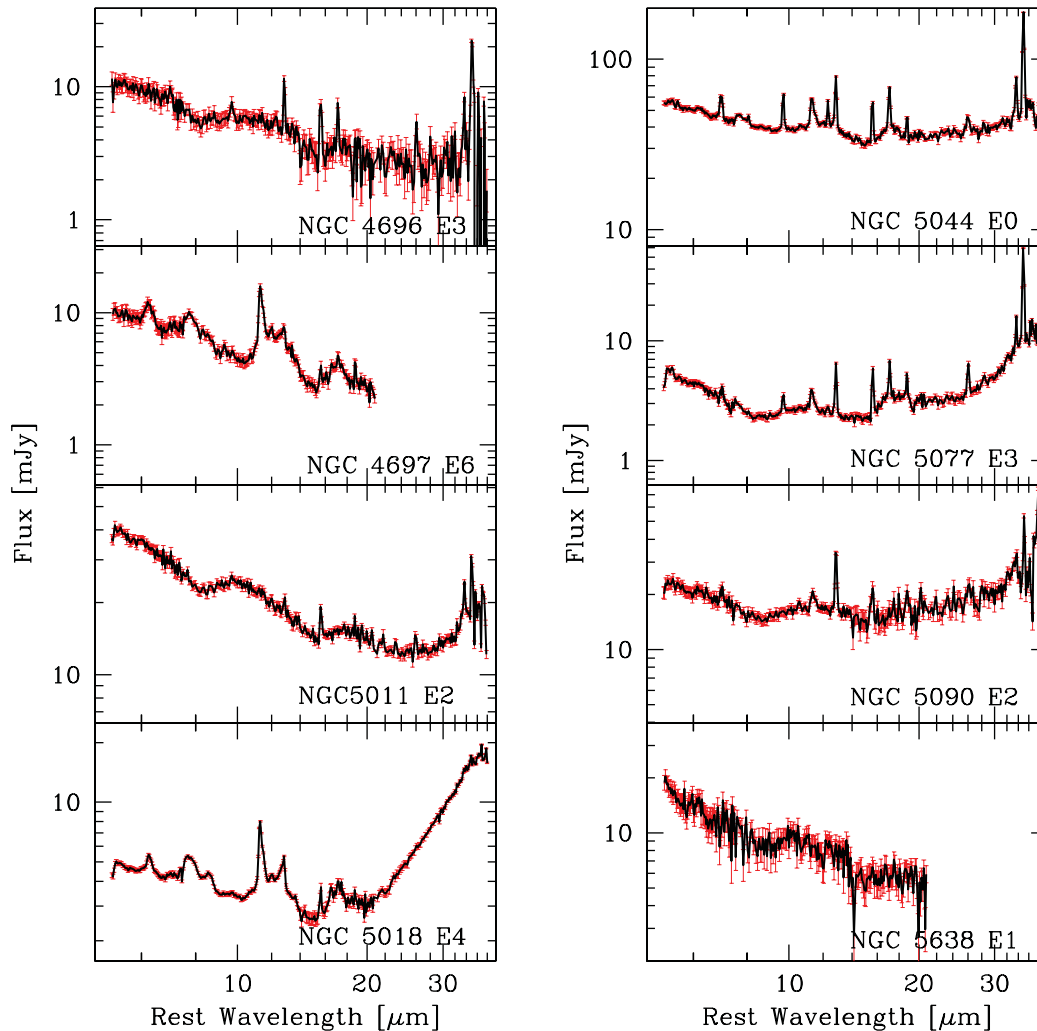
Figure 1 – *continued*

The bottom panel of Fig. 4 shows the discrimination offered by the 7.7-µm/11.3-µm PAH ratio in disentangling active MIR classes 2, 3 and 4. All class-2 nuclei have anomalous 7.7-µm/11.3-µm PAH ratios and 6-µm/15-µm values higher than NGC 4261. All but one class-3 ETGs are located in the typical starburst region (solid horizontal lines) (Smith et al. 2007). NGC 3268 is borderline between class-3 and class-2, as its 7.7-µm/11.3-µm PAH ratio = 2.3. NGC 5128 has both a high 6-µm/15-µm excess and a 7.7-µm/11.3-µm PAH ratio typical of star-forming galaxies (see next section).

The results of our MIR spectral classification are collected in Table 5. In Fig. 5 we provide a synoptic view of all ETG nuclei in classes 3 and 4.

4.3 Individual notes about MIR classification

NGC 4261 (E3) This galaxy (see Fig. 4) is borderline between class-4 and class-2. It displays a MIR spectrum similar to that of NGC 4486 (see Fig. 5). In contrast to NGC 4486, the spectrum of this galaxy shows the high-ionization [Ne V] 14.32-µm emission line, and it is probable that a dusty torus is needed to fully account for the observed continuum, in addition to a synchrotron component.

NGC 4383 (S0) This galaxy was included in MIR class-3 because of its PAH inter-band ratio (7.7-µm/ 11.3-µm = 4.6). However, it presents the steepest and strongest MIR continuum of any ETG in class-3. The analysis of the spectrum shows that the slope of the MIR continuum, calculated as $F_\nu(30\,\mu m)/F_\nu(15\,\mu m) = 6.7$, is consistent with the values found in starburst galaxies (see e.g. Brandl et al. 2006). Furthermore, the [Ne III] 15.5-µm /[Ne II] 12.8-µm versus [S III] 33.5-µm/ [Si II] 34.8-µm diagnostic diagram (see Dale et al. 2006) locates the galaxy in the starburst region. All of these indicate that the class-3 classification points to the presence of ongoing star formation in the nucleus.

The lower values of the MIR slopes shown by the remaining class-3 objects in Fig. 5 (2.3 for NGC 3258, 1.2 for NGC 3268, 4.2 for NGC 5018 and 4.5 for NGC 4435; Panuzzo et al. 2007) may indicate that the starburst phase in these objects is fading and that there are not as many ionizing stars to heat the dust as in the peak of the starburst phase. This has been discussed in some detail by Panuzzo et al. (2007) for the case of NGC 4435.

NGC 5128 Cen A (S0+S pec) The most striking feature in the IRS spectrum of this galaxy is the strong silicate absorption feature at 9.7 µm. This feature is weak or seen in emission in the other class-4 galaxies of the sample. Sargsyan et al. (2011) found this feature typical of the so-called 'absorption AGN' while 'emission
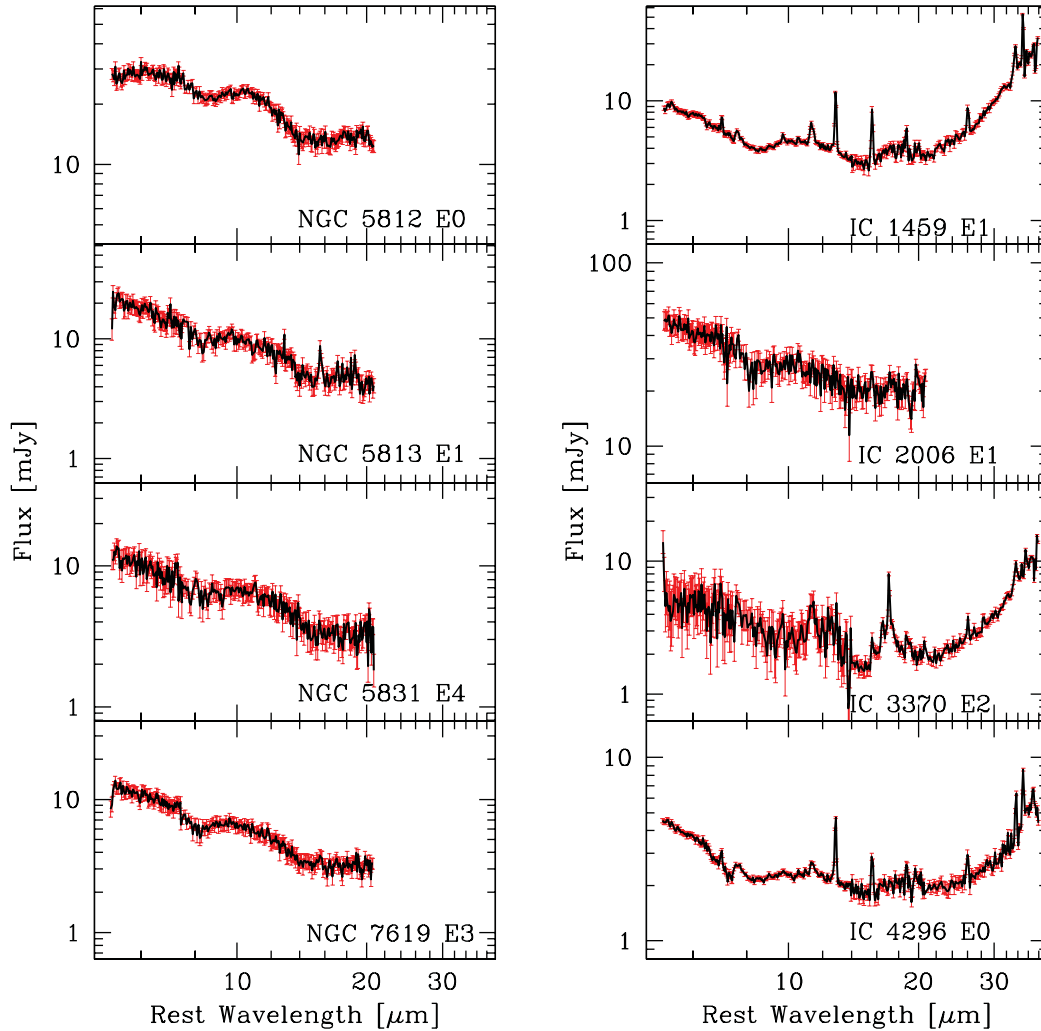
Figure 1 – *continued*

AGN' have spectra similar to our MIR class-4 spectra. Such a strong absorption is an indication of an enormous amount of extinction towards the nucleus, which is probably embedded in a very dusty and compact torus (see e.g. Armus et al. 2007).

NGC 5273(S0/a) This galaxy was included in class-4 because of its large MIR excess over the underlying stellar population continuum. Unfortunately, the spectrum does not include the SL2 module (see Table 4).

5 DEMOGRAPHY OF MIR SPECTRAL PROPERTIES OF ETGS

In the following subsections we investigate the MIR spectra and their classes as a function of the properties of the host galaxy in a multiwavelength context. Adopting Poisson statistics, for each percentage we obtained single-sided upper and lower limits, corresponding to 1σ Gaussian errors (Gehrels 1986).

### 5.1 MIR classes versus morphological classification and galaxy environment

We summarize the data concerning MIR classes versus E and S0 morphological classes and the galaxy environment in Table 6.

Es are significantly more passive than S0s: 46^{+11}_{-10} per cent of Es and 20^{+11}_{-7} per cent of S0s have a class-0 spectrum.

S0s show a tendency to be more gas-rich than Es: 80^{+18}_{-15} per cent of S0s and 54^{+11}_{-10} per cent of Es belong to classes 1, 2, 3 and 4, showing emission lines. Considering the whole sample of ETGs, 64^{+12}_{-6} per cent of the nuclei show emission lines, although with different intensities. This is in agreement with optical studies, in which, depending on the sample (sometimes strongly biased against passively evolving objects), ionized gas is detected in ∼50–90 per cent of ETGs (Phillips et al. 1986; Macchetto et al. 1996; Sarzi et al. 2006, 2010; Yan et al. 2006; Serra et al. 2008; Annibali et al. 2010).

A total of 41^{+10}_{-9} per cent of Es and 57^{+16}_{-13} per cent of S0s show PAH emission, indicating that in about half (47^{+8}_{-7} per cent) of ETGs a star formation episode occurred about 10^8 years ago (Kaneda et al. 2008; Panuzzo et al. 2011). Galaxies with normal PAH ratios, class-3 spectra, are a minority amongst both Es and S0s: only 9^{+4}_{-3} per cent show star-forming spectra.

Panuzzo et al. (2011) considered the ratio between the class-2 and class-3 spectra while investigating the hypothesis that anomalous PAHs in class-2 are produced by carbon stars (Vega et al. 2010). For solar metallicity, carbon stars are present in stellar populations with ages between ∼250 Myr and ∼1.3 Gyr (Marigo & Girardi 2007). Assuming a characteristic lifetime of 200 Myr for a star
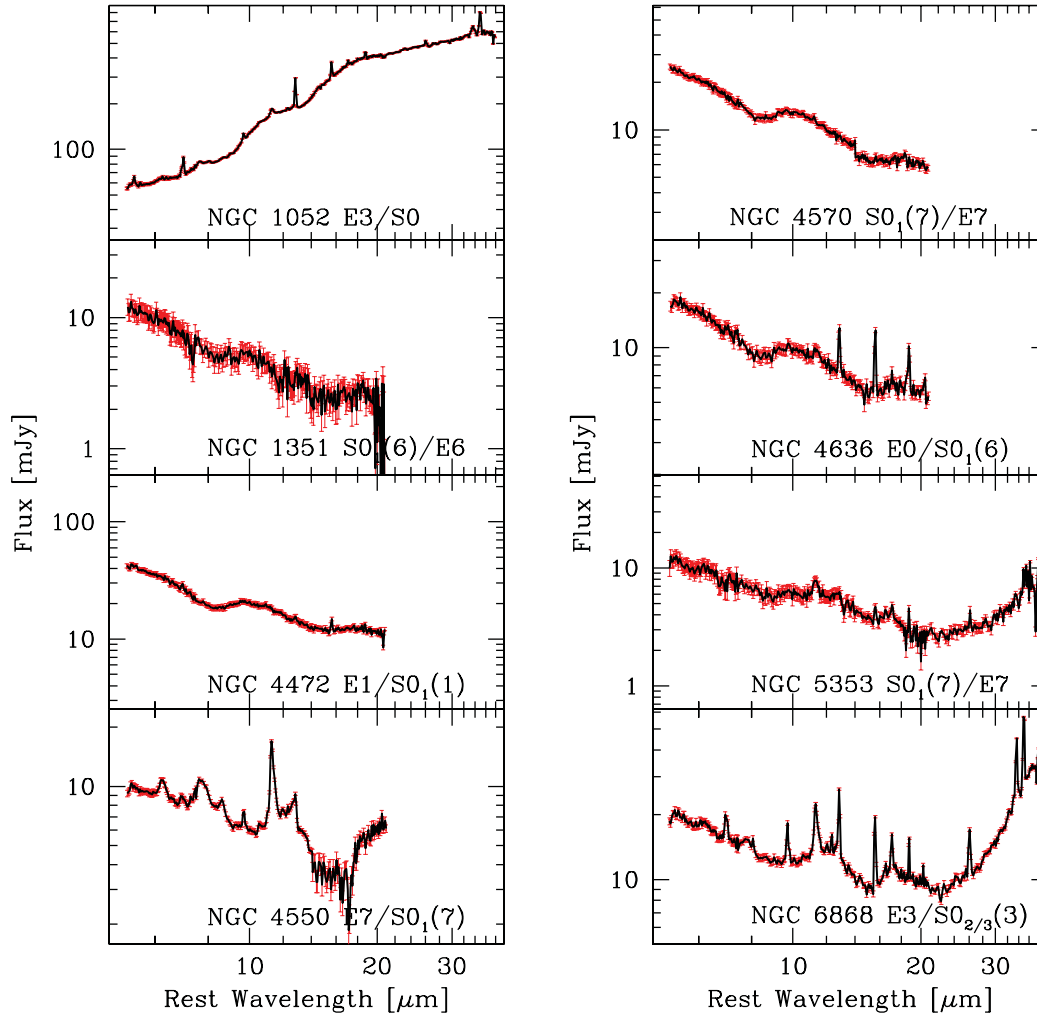
Figure 1 – *continued*

formation episode (Panuzzo et al. 2007), the expected ratio between the number of ETGs with anomalous PAH (class-2) with respect to the number of ETGs with normal PAHs (class-3) should be in the range 1 to 7. Here we obtain a ratio of 3.5, half of that reported in Panuzzo et al. (2011).

All MIR class-4 spectra show PAHs, suggesting that the AGN phenomenon is associated with star formation. Class-4 MIR spectra (Fig. 5, bottom panel) include three E and four S0 galaxies, corresponding to 8^{+4}_{-3} per cent of our ETG sample.

The fraction of Es with PAH features (classes 2, 3 and 4) in clusters tends to be lower than that in LDEs (20^{+19}_{-11} per cent versus 49^{+13}_{-11} per cent), suggesting that star formation episodes are triggered in LDEs. The PAH features of S0s show a similar percentage in clusters and in LDEs (44^{+23}_{-16} per cent versus 68^{+25}_{-19} per cent). These results are consistent with other indicators that find ETGs located in high-density environments that are older (Clemens et al. 2006, 2009) and, in general, less 'active' (Moore et al. 1996; Feldmann, Carollo & Mayer 2011, for theoretical approaches) than their counterparts in groups and in the field.

5.2 MIR classes and the hot nuclear gas

In the top panel of Fig. 6, we plot the nuclear X-ray luminosity, $L_{X, nuc}$ versus the MIR class. The $L_{X, nuc}$ (Table B1, columns 4 and

9; Pellegrini 2010) refers to a central aperture ($\sim$2-arcsec radius) in the 2–10 keV bands of *Chandra* observations (Pellegrini, private communication). The $L_{X, nuc}$ aperture lies within the *Spitzer*–IRS slit width and allows us to investigate the presence of the AGN engine and the role of the X-ray radiation field on MIR spectra.

ETGs in class-4 have higher values of $L_{X, nuc}$, as expected from the presence of an AGN. An analysis of X-ray spectra in a subsample of our ETGs, obtained with *Chandra* and *XMM–Newton* data, shows that a power-law component is needed to account for the observed emission of all ETGs in class-4 (González-Martín et al. 2009; Boroson, Kim & Fabbiano 2011; Machacek, Jones & Forman 2004; Capetti & Balmaverde 2006; Grützbauch et al. 2007; Ghosh et al. 2005).

ETGs in class-0 show low values of $L_{X, nuc}$ ($\sim$$10^{38}$–$10^{39}$ erg s^{-1}, see Fig. 6), with some exceptions. An X-ray spectral analysis of the class-0 NGC 720, 821 and 1399 shows the need for an AGN contribution, in contrast to the case for NGC 1427, 3379, 3377, 3608 and 4473. Pellegrini (2010) remarks on the large spread of $L_{X, nuc}$ and suggests that it could be produced by the nuclear activity cycle, where $L_{X, nuc}$ is regulated by the joint actions of the feedback and the fuel availability.

High values of $L_{X, nuc}$ are also found in ETGs of classes 1 and 2 and in some of class-3, probably reflecting the contribution of an AGN. In particular, an AGN contribution has been detected
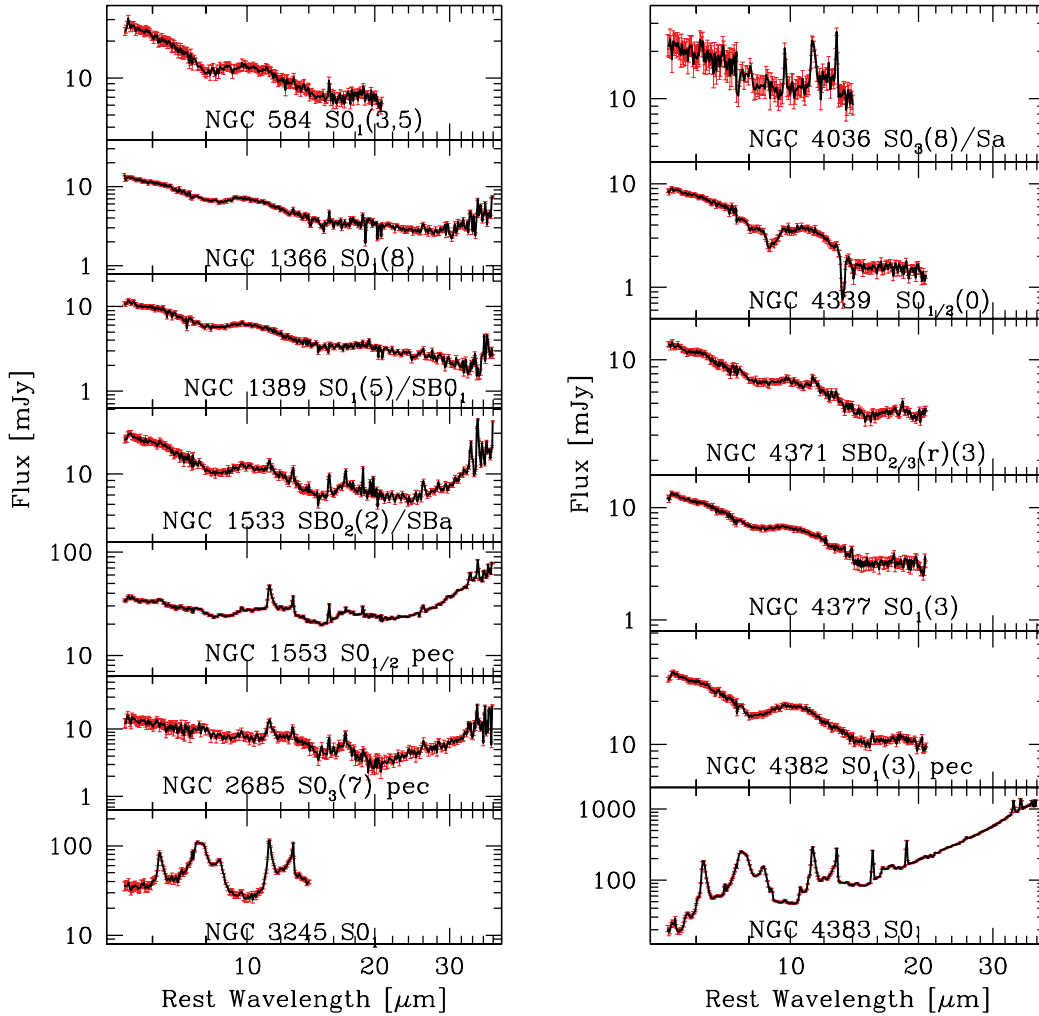
Figure 1 – *continued*

in the X-ray spectra of NGC 1404, 4649 and 5846 of class-1; in NGC 1553, 2685, 4036, 4374, 4552, IC 1459 and NGC 5090 of class-2; and in NGC 3245, 4435, 4697 and 5018 of class-3. No AGN contribution is required to model the X-ray spectra of NGC 584 (class-1) or of NGC 4589 and 4696 (class-2).

X-ray cavities are considered signatures of the AGN feedback (Cavagnolo et al. 2010, and references therein). *Chandra* observations detected X-ray cavities in many of our ETGs (NGC 3608 in class-0; NGC 4472, 4649, 5813 and 5846 in class-1; NGC 1553, 4552, 4636, 5044 and IC 4296 in class-2; NGC 4261 in class-4), suggesting an evolutionary link between MIR classes.

5.2.1 11.3-μm/7.7-μm PAH ratio and the hot nuclear gas

In the bottom panel of Fig. 6, we plot the ratio between the PAH features at 11.3 μm and 7.7 μm versus $L_{X, nuc}$. Although the dispersion is quite large, the figure shows a weak relation (the Pearson correlation coefficient is $r = 0.58$) between the PAH 11.3-μm/7.7-μm ratio and $L_{X, nuc}$. Draine & Li (2007) suggested that variations in PAH emission ratios can be accounted for by the combined effects of variations in exciting radiation, PAH size and ionization state. The nuclear X-ray radiation field seems indeed to play a role in the determination of the PAH 11.3-μm/7.7-μm ratio, taking into account the large variation of $L_{X, nuc}$ reported by Pellegrini (2010). ETG nuclei

in class-3 (normal PAH ratios) have a lower $L_{X, nuc}$ emission than ETGs with anomalous PAH ratios, as shown by the median values (large open squares in Fig. 6 bottom panel) of classes 2 and 4.

5.3 MIR classes, MIR atomic line diagnostics and H₂ emission

Table B1 (columns 3 and 8) reports the optical activity class of the ETG nuclei (Ho, Filippenko & Sargent 1997; Annibali et al. 2010). A large fraction of them are LINERs in the optical window, as they show low-ionization emission lines. Among optical LINERs, MIR classes identify both passively evolving ETGs and star-forming nuclei well (Rampazzo et al. 2011, their fig. 2). However, what powers the remaining objects of the vast class of LINERs is still debated.

In Fig. 7, MIR classes 1 to 4 are plotted in the Ne[III]15.5-μm/[Ne II]12.8-μm versus [S III]33.5-μm/[Si II]34.8-μm plane (Dale et al. 2006). The plot indicates the areas in which AGNs, LINERs and starburst galaxies are typically located. Similarly to in optical diagnostic diagrams (e.g. Annibali et al. 2010), the MIR line diagnostic is unable to fully separate powering mechanisms. ETGs in class-3, except for NGC 3258, inhabit the starburst sector, mixed together with class-2 galaxies, although the two classes have totally different PAH ratios, that is, different star-forming properties. ETGs in class-2 also mix with those in class-4, suggesting the presence
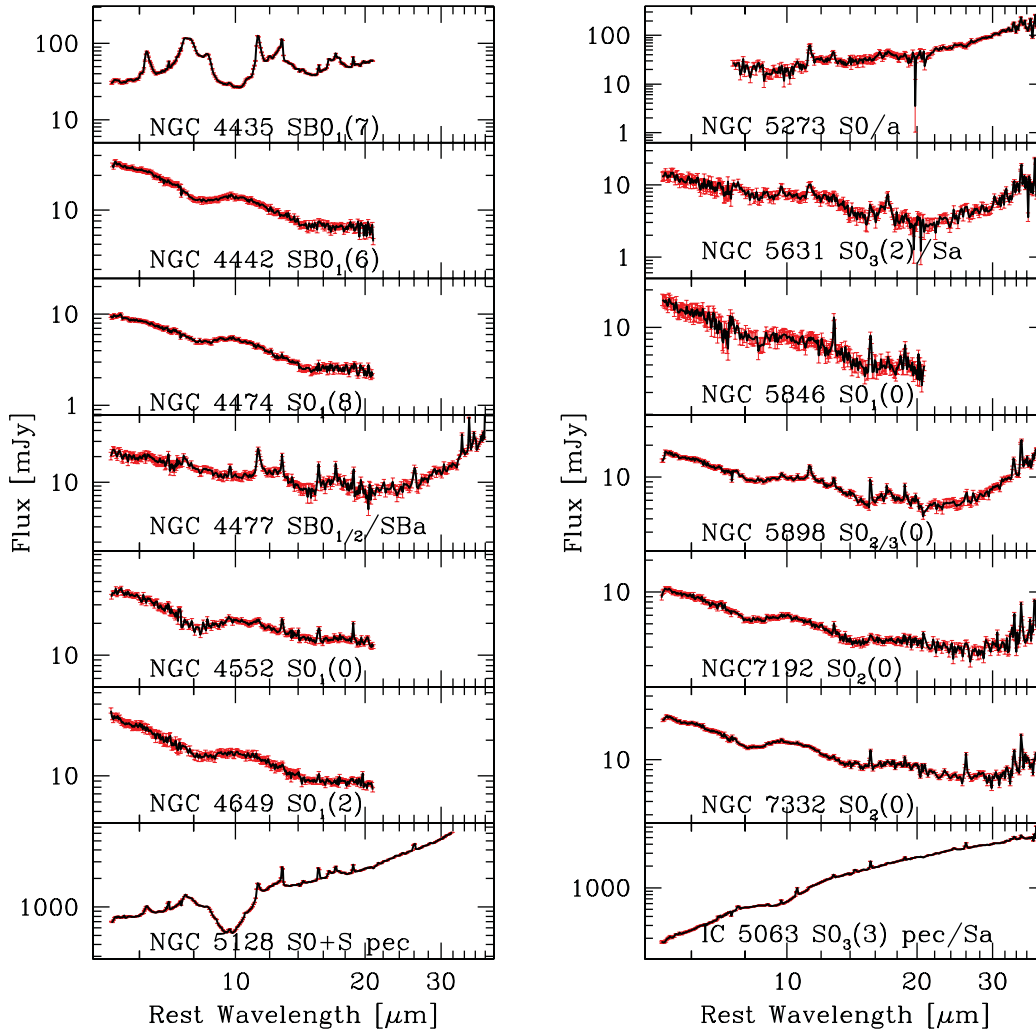
Figure 1 – *continued*

of an AGN contribution. The class-4 NGC 4261, a LINER in the optical, is located in the starburst region of Fig. 7. In the MIR, its AGN nature is suggested by the presence of an excess over the passive stellar continuum, similarly to NGC 4486, and by the high-ionization [NeV] 14.32-μm emission line, as well as, in the X-ray, by the detection of a central AGN and cavities.

In the current literature, low-accretion-rate AGNs are the favoured mechanism for ionizing LINERs. Considering that massive black holes are thought to be present in galaxies with a spheroidal component (e.g. Kormendy et al. 2004), the above mechanism is supported by the presence of compact X-ray and/or nuclear radio sources (González-Martìn et al. 2009), UV and X-ray variability (Maoz et al. 2005; Pian et al. 2010) and broad emission lines in the optical spectra. However, there is evidence for a deficit of ionizing photons from weak AGNs, suggesting that more than one excitation mechanism may operate in LINERs (see Eracleous, Hwang & Flohic 2010). Furthermore, the photoionization by old post-asymptotic giant branch (post-AGB) stars (Trinchieri et al. 1991; Binette et al. 1994; Stasińska et al. 2008) can account for the ionizing photon budget only in the weakest LINERs, or in off-nuclear regions (Annibali et al. 2010).

For a long time, shocks (Koski et al. 1976; Heckman 1980; Dopita et al. 1995; Allen et al. 2008) have been proposed as a possible gas ionization mechanism in ETG nuclei. The shock scenario may be related to the presence of the H_2 molecular emission that is thought to be an important coolant in post-shock regions (Roussel et al. 2007; Ogle et al. 2007). We found the $H_2 S(1)$ line with similar rates in Es (34^{+10}_{-8} per cent) and S0s (51^{+15}_{-12} per cent). Several galaxies with X-ray cavities indeed show H_2 emission, such as NGC 1553, 4374, 4552, 4636, 5044, 5813 and IC 4296, as do MIR class-4 galaxies with X-ray-detected AGNs, such as NGC 1275, 1052, 4036 and 5128. However, the largest fraction of H_2 emitters is found among MIR class-2 galaxies.

5.4 MIR classes and CO

In this section we report on CO observations, with the aim of investigating MIR class versus ETG cold-gas content.

In total, 41 galaxies of our sample are included in the survey of 260 ETGs in ATLAS^{3D} (Young et al. 2011). Only 6 out of the 41 (15^{+9}_{-6} per cent) were detected: four (NGC 4036, 4435, 4477, 5273) in both CO $J = 1$–0 and $J = 2$–1 and two (NGC 2685 and 3245) in the $J = 1$–0 line. Detected galaxies are S0s, and none belongs to MIR class-0 or class-1. NGC 2685, 4036 and 4477 are of MIR class-2; NGC 3245 and 4435 are of class-3; and NGC 5273 is of
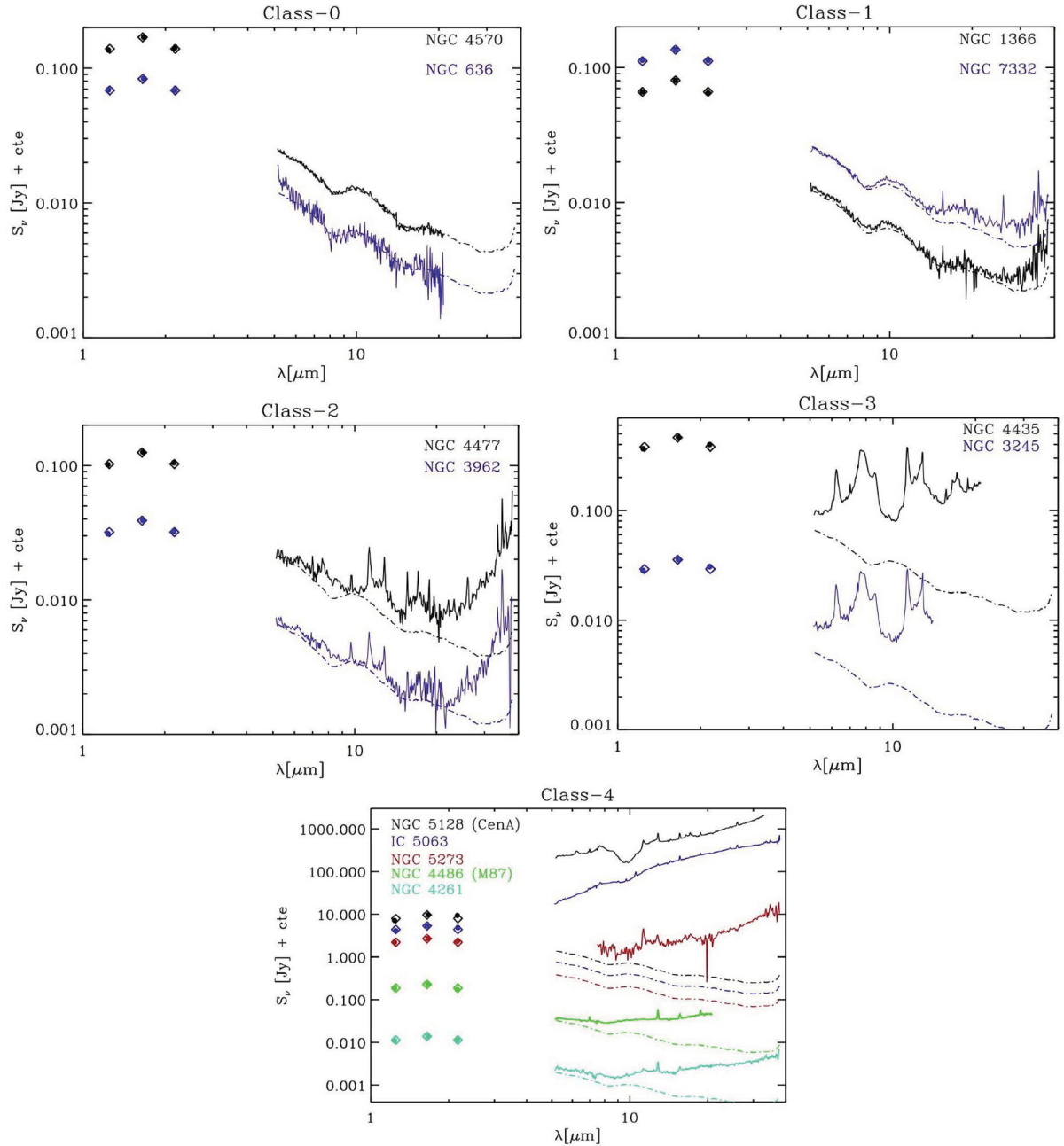
Figure 2. Comparison of the passive template used in this work (dot–dashed line) and the mid-infrared (MIR) spectra (solid line) of various galaxies with different degrees of MIR activity. The template has been normalized to the *H*-band flux of each galaxy. The 2MASS *J*-, *H*- and *K*-band fluxes of the galaxies, within the central 5-arcsec radius, are indicated by filled circles, while the corresponding normalized values of the template are plotted as open diamonds.

class-4. Their molecular gas masses are in the range $7.27 < \log M(\mathrm{H_2}) < 8.13$ $\mathrm{M_\odot}$ (Young et al. 2011).

NGC 4550 and 4697 of class-3 are undetected in Young et al. (2011). Wiklind & Henkel (2001) and Sofue & Wakamatsu (1993) detected NGC 4550 and 4697 (together with the class-2 NGC 4589), respectively, in the CO $J = 1$–0 line. The class-3 S0 NGC 4383 is also detected in this line (Thronson et al. 1989).

NGC 4261 and 4486, in class-4, were undetected by Young et al. (2011) (see also Ocaña Flaquer et al. 2010 for NGC 4261). Smolčić & Riechers (2011) detected NGC 4486 in the $J = 1$–0 line. Several ETGs of class-4 have been detected in CO, namely NGC 1052 (Welch, Sage & Young 2010, $J = 2$–1), NGC 1275 (Salomé et al. 2006) and NGC 5128 (Morganti 2010) and IC 5063 (Morganti

et al. 2013, in CO $J = 2$–1). Their $\mathrm{H_2}$ masses differ by orders of magnitude, scaling down from about 10^{10} $\mathrm{M_\odot}$ in NGC 1275, to 10^8 $\mathrm{M_\odot}$ in NGC 5128 and IC 5063, and to about 10^7 $\mathrm{M_\odot}$ in NGC 1052.

In summary, all ETGs detected in CO lines show PAHs, either with normal or anomalous ratios, in their MIR nuclear spectra.

5.5 MIR classes and the radio continuum at 1.4 GHz

A large fraction of ETGs in the present sample are radio-emitters, although with different radio intensities, morphologies and classes. In Table B1 (columns 5 and 10) we report the 1.4-GHz radio power catalogued by Brown et al. (2011). These authors found that the radio
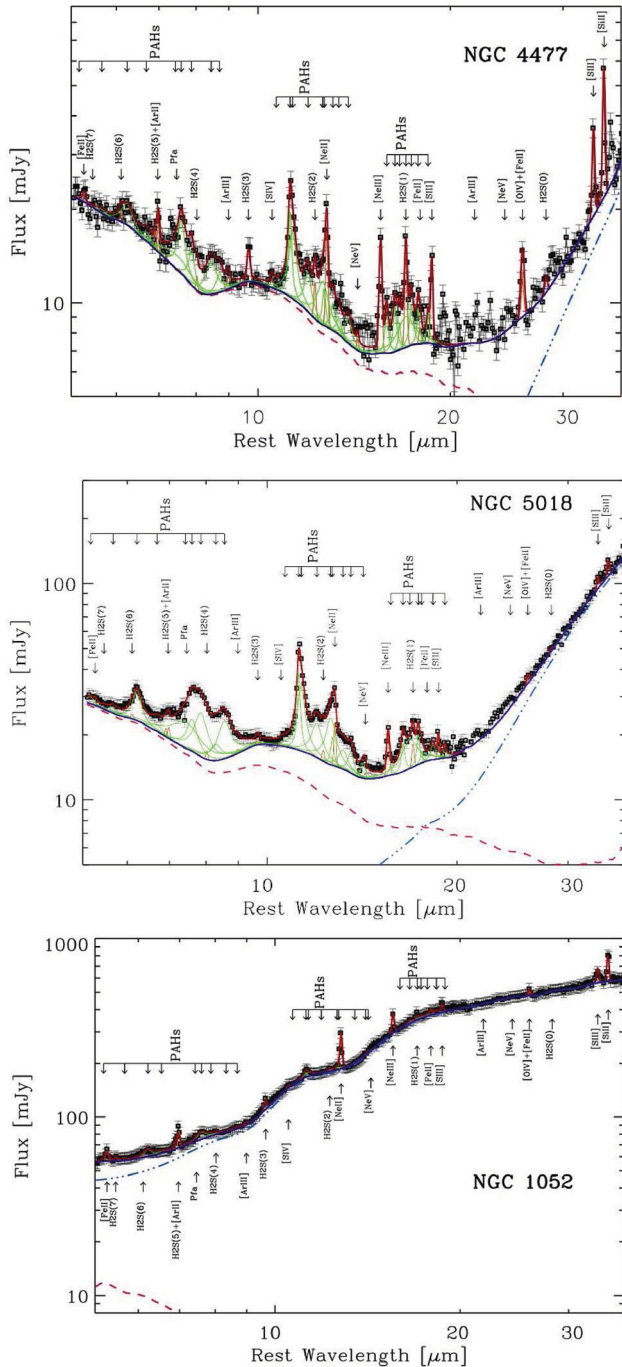
Figure 3. Best fit of the spectrum of three early-type galaxies with anomalous polycyclic aromatic hydrocarbon (PAH) emissions (upper panel), normal PAH emissions (middle panel), and a steep mid-infared (MIR) continuum (bottom panel). Open squares and the solid thick red line are the observed MIR spectra and our final best fit, respectively. The fit is calculated as the sum of an underlying continuum (solid thick blue line), the PAH features (solid thin green line) and the emission lines (solid thin orange line). The two components of the continuum, namely the old stellar population (dashed red line) and diffuse dust emission (dot–dashed blue line), are also plotted.

power of ETGs with similar M_K magnitude may vary by roughly two orders of magnitude over long periods of time. The radio power may keep trace of the past activity (AGN and/or star formation), which is useful for investigating the possible link between MIR classes.

Fig. 8 (top left panel) shows the distribution of the 1.4-GHz radio power versus M_K magnitude. All ETGs brighter than -25.2 mag are detected. According to Brown et al. (2011), massive galaxies always host an AGN or have recently undergone star formation. The top right panel of Fig. 8 shows M_K magnitude versus MIR class. Each MIR class covers roughly the full range of M_K.

Consideration of $P_{1.4\,\mathrm{GHz}}$ versus MIR class suggests the following. Although having a large dispersion, class-4 includes the more powerful radio sources (Fig. 8, bottom panel). Star-forming, class-3, ETGs have intermediate/low radio power. A star formation rate of $\sim 1\,\mathrm{M_\odot\,yr^{-1}}$ is expected to produce $10^{21}\,\mathrm{W\,Hz^{-1}}$ of radio emission in ETGs (Wrobel & Heeschen 1988; Bell 2003). The Milky Way (indicated in the plot) has a radio power $P_{1.4\,\mathrm{GHz}} \simeq 4 \times 10^{21}\,\mathrm{W\,Hz^{-1}}$. In class-2, the stronger radio-emitters are ETGs with X-ray cavities, probably connected to the AGN feedback (Cavagnolo et al. 2010). X-ray cavities are also detected in class-1 and in the E of class-0, NGC 3608 ($M_K = -24.80$), detected at 1.4 GHz.

ETGs in class-0 set the lower boundary of the $P_{1.4\,\mathrm{GHz}}$ radio power. Remarkable exceptions are NGC 1407 and 1399. These are among the brightest ($M_K \leq -25.3$) Es in the sample, and have radio jets (Van Velzen et al. 2012) and X-ray-detected AGNs in their nuclei (Pellegrini 2005). A misalignment of the SL and LL slits with respect to the jet position angle may explain the class-0 spectrum of these galaxies. In the case of NGC 4486, the jet is sampled only by the LL slits; notwithstanding this, Buson et al. (2009) detected synchrotron emission.

6 MIR CLASSES AND ACCRETION SIGNATURES

Panuzzo et al. (2011) suggested that an accretion event may cause a passively evolving ETG (class-0) to ignite star formation (class-3) and/or feed the central black hole, revitalizing the AGN activity (class-4). We review here possible accretion signatures, such as peculiarities in the morphology and kinematics of the galaxy and of the dust-lane structure.

6.1 Morphological and kinematical peculiarities

In Tables B2 and B3 we collect the kinematical (column 3) and morphological (column 4) peculiarities described in the literature for Es and S0s, respectively. The kinematical notes consider the detection of counter-rotation (CR), gas versus gas, stars versus gas and stars versus stars, and of multiple kinematical components (MC), widely believed to be associated with accretion events (see e.g. Corsini et al. 1998; Krajnović et al. 2008; Bois et al. 2012). Other kinematical peculiarities are reported, such as rotation along the minor axis, a phenomenon often associated with galaxy triaxiality (Bertola et al. 1988). The morphological peculiarities include the detection of shells, tidal tails, peculiar isophote shapes that are believed to be associated with interaction and/or minor/major merger events (Thomson & Wright 1990; Thomson 1991; Dupraz & Combes 1986; Henquist & Quinn 1987a,b).

In total, 41^{+8}_{-7} per cent of ETGs show some form of kinematical peculiarity. The percentage is probably a lower limit, as some galaxies do not have detailed kinematical studies. Many galaxies also show morphological peculiarities. The above rate is consistent with the findings (53^{+10}_{-4} per cent) of van Dokkum (2005) obtained from the analysis of morphological peculiarities in a comparable sample of nearby ETGs. He concludes that the majority of today's most luminous Es in the field were assembled through mergers of gas-poor, bulge-dominated systems. However, the high fraction of
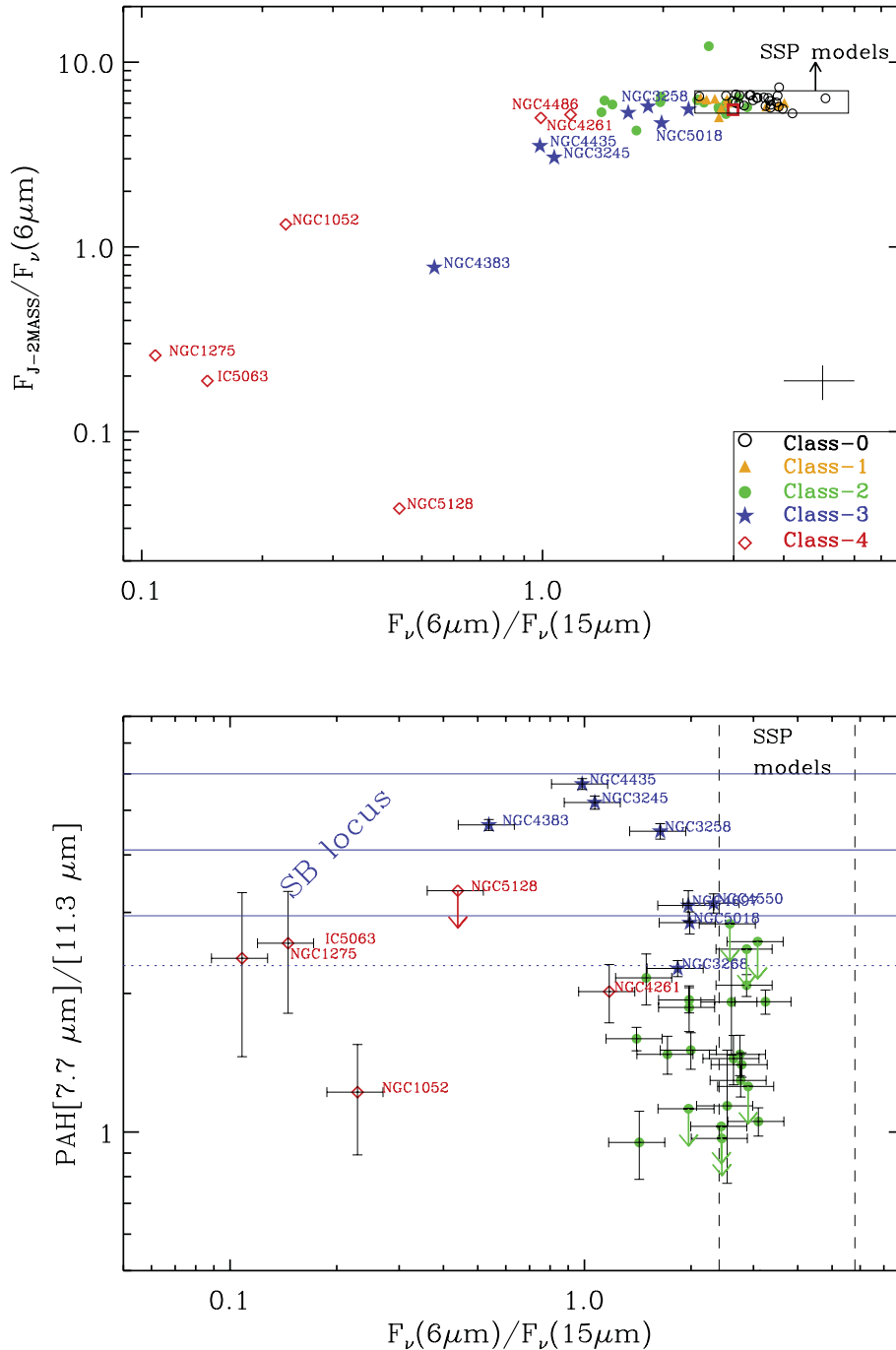
Figure 4. (Top panel) Colour–colour plot of the 2MASS *J*-band/6-μm versus the 6-μm/15-μm flux ratios. The rectangle encloses single stellar population (SSP) models of early-type galaxies with ages in the interval 10–14.5 Gyr and metallicty, *Z*, in the range 0.004–0.05. The red open square within the rectangle represents a 12-Gyr-old SSP model with solar metallicity. The typical error is also shown. (Bottom panel) The 7.7-μm/11.3-μm PAH ratio versus the 6-μm/ 15-μm flux ratio. The dotted horizontal line corresponds to cirrus emission (Lu et al. 2003). Solid horizontal lines mark the region of the H II-dominated sources or starburst galaxies (SB); the central line is the median 4.2 value (Smith et al. 2007). The dashed vertical lines mark the area of old SSP models described above.

ETG nuclei with line emission that we found (64_6^{12} per cent) argues that the above 'dry merger' scenario is not so relevant.

Although column 4 in Tables B2 and B3 is largely incomplete, owing to a still limited number of 2D kinematical studies, it is evident that kinematical (and morphological) signatures of accretions are found also in passively evolving Es and S0s (e.g. NGC 3377, 3608, 4570, 4621, 4660, 5831). The fact that ETGs in class-0

show kinematical/morphological peculiarities suggests that these are long-lasting structures with respect to spectroscopic features: galaxies were active in the recent past, as traced by the peculiar kinematics/structures, but their spectra have already evolved into a passive phase (see e.g. Longhetti et al. 2000, for shell galaxies). Another possibility is a 'dry' (van Dokkum 2005) and *sterile* accretion; that is, one that did not induce a star formation/AGN episode.

Table 5. MIR spectral classes.

Galaxy	RSA morph. type	MIR class	Galaxy	RSA morph. type	MIR class
NGC 636	E1	0	NGC 5090	E2	2
NGC 720	E5	0	NGC 5638	E1	0
NGC 821	E6	0	NGC 5812	E0	0
NGC 1209	E6	1	NGC 5813	E1	1
NGC 1275	E pec	4	NGC 5831	E4	0
NGC 1297	E2	2	NGC 7619	E3	1
NGC 1339	E4	0	IC 1459	E1	2
NGC 1374	E0	0	IC 2006	E1	1
NGC 1379	E0	0	IC 3370	E2 pec	2
NGC 1395	E2	2	IC 4296	E0	2
NGC 1399	E1	0			
NGC 1404	E2	1	NGC 1052	E3/S0	4
NGC 1407	E0	0	NGC 1351	$S0_1$/E6	0
NGC 1426	E4	0	NGC 4472	E1/$S0_1$	1
NGC 1427	E5	0	NGC 4550	E/S0	3
NGC 1453	E2	2	NGC 4570	E7/$S0_1$	0
NGC 1549	E2	2	NGC 4636	E0/$S0_1$	2
NGC 1700	E3	1	NGC 5353	$S0_1$/E7	2
NGC 2300	E3	0	NGC 6868	E3/$S0_{2/3}$	2
NGC 2974	E4	2	NGC 584	$S0_1$	1
NGC 3193	E2	0	NGC 1366	$S0_1$	1
NGC 3258	E1	3	NGC 1389	$S0_1$/$SB0_1$	0
NGC 3268	E2	3	NGC 1533	$SB0_2$/SBa	2
NGC 3377	E6	0	NGC 1553	$S0_{1/2}$ pec	2
NGC 3379	E0	0	NGC 2685	$S0_3$ pec	2
NGC 3557	E3	2	NGC 3245	$S0_1$	3
NGC 3608	E1	0	NGC 4036	$S0_3$/Sa	2
NGC 3818	E5	0	NGC 4339	$S0_{1/2}$	0
NGC 3904	E2	0	NGC 4371	$SB0_{2/3}$(r)	2
NGC 3962	E1	2	NGC 4377	$S0_1$	0
NGC 4261	E3	4	NGC 4382	$S0_1$ pec	1
NGC 4365	E3	0	NGC 4383	S0:	3
NGC 4374	E1	2	NGC 4435	$SB0_1$	3
NGC 4473	E5	0	NGC 4442	$SB0_1$	0
NGC 4478	E2	0	NGC 4474	$S0_1$	0
NGC 4486	E0	4	NGC 4477	$SB0_{1/2}$/SBa	2
NGC 4564	E6	0	NGC 4552	$S0_1$	2
NGC 4589	E2	2	NGC 4649	$S0_1$	1
NGC 4621	E5	0	NGC 5128	S0+S pec	4
NGC 4660	E5	0	NGC 5273	S0/a	4
NGC 4696	E3	2	NGC 5631	$S0_3$/Sa	2
NGC 4697	E6	3	NGC 5846	$S0_1$	1
NGC 5011	E2	1	NGC 5898	$S0_{2/3}$	2
NGC 5018	E4	3	NGC 7192	$S0_2$	1
NGC 5044	E0	2	NGC 7332	$S0_{2/3}$	1
NGC 5077	E3	2	IC 5063	$S0_3$/Sa	4

Despite the presence of kinematical/morphological distortions, the spectrum remains passive, as in the case of an unperturbed/quiescent galaxy.

6.2 Dust-lane peculiarities

In column 5 of Tables B2 and B3 a description of the observed dust-lanes in the nuclear region is provided. The dust-lane morphology is available for 48/56 Es and for 25/35 S0s. 50^{+12}_{-11} per cent of Es and 32^{+16}_{-11} per cent of S0s do not show dust-lanes.

Dust in ETGs, including the most passive objects, is normally produced by the collective outflow of dusty gas from evolving AGB stars. The silicate emission from this dust explains the 10-μm feature seen in MIR ETG spectra (Knapp et al. 1989; Athey et al. 2002).

However, the short lifetime of dust in the ETG environment means that little dust can accumulate unless it is somehow shielded from the hot gas (Clemens et al. 2010). In addition, the distribution of this dust follows that of stars, so dust-lanes cannot be produced in this way.

The presence of dust-lanes and their asymmetries therefore points to an external origin for the dust. An external origin is also consistent with (i) the lack of any strong correlation between far-IR and optical galactic luminosities (e.g. Forbes 1991; Goudfrooij & de Jong 1995; Trinchieri & Goudfrooij 2002); (ii) the warm, counter-rotating gas observed in some ETGs (see Tables B1 and B2); (iii) the distorted morphology of the dust (e.g. Finkelman et al. 2012).

In 42^{+18}_{-13} per cent of Es and 24^{+14}_{-9} per cent of S0s the dust-lane morphology is irregular or chaotic. Dust-lanes are often associated with morphological and/or kinematical peculiarities. Irregular/chaotic dust-lanes are found in all MIR classes. Dust-lanes, some quite complex, are found in class-4 (NGC 1052, 1275, 5128, 5273 and IC 5063). Some Es, such as NGC 1407, 4621, 4660 and 5831, with MIR class-0 spectra, do not have dust-lanes detected in the optical but display kinematical peculiarities, such as counter-rotation or rotation along the apparent minor axis, suggesting that either dry accretion events or dust evaporation may have occurred.

7 SUMMARY AND CONCLUSIONS

We present homogeneously reduced and calibrated low-resolution, *Spitzer*–IRS spectra of a sample of 91 ETGs ($T < 0$) in the Revised Shapely–Ames Catalog (Sandage & Tammann 1987). We aim to provide a MIR atlas of well-studied, nearby ETGs in the range ~5–40μm.

The atlas provides a measure of the atomic and molecular emission lines and PAH intensities. We classify each spectrum into one of the five MIR spectral classes devised by Panuzzo et al. (2011) for characterizing passive (class-0), intermediate (class-1 and class-2), star-forming (class-3) and AGN (class-4) nuclei. The main results are as follows.

(i) The nuclei of ~1/3 (36^{+7}_{-6} per cent) of nearby ETGs in the atlas have a MIR class-0 spectrum, namely passively evolving according to Bressan et al. (2006). Class-0 spectra are more frequently detected among Es than among S0s (46^{+11}_{-10} per cent versus 20^{+11}_{-7} per cent). ETGs in class-0 set the lower boundary of the $P_{1.4\,GHz}$ radio power; that is, they are the most quiescent nuclei, on average. Relevant exceptions are the massive ($M_K < -25.2$) class-0 Es in Fornax, NGC 1399 and NGC 1407, both having a high $P_{1.4\,GHz}$ and a radio jet.

About 78^{+22}_{-18} per cent of Es and all S0s in class-0 show no dust-lanes in the optical, although some galaxies show kinematical and morphological distortion, pointing to the occurrence of a past accretion episode. Thus, class-0 ETGs include either genuinely unperturbed, passively evolving galaxies or systems in which the effect of accretion has already been quenched.

(ii) Emission lines are detected in 64^{+12}_{-6} per cent of nuclei. The detection of emission lines in many galaxies that show kinematical evidence of merger events argues against the so-called 'dry mergers' being an important formation mechanism for ETGs. H_2 molecular lines are also frequently detected: the $H_2S(1)$ emission line is detected in 34^{+10}_{-8} per cent of Es and 51^{+15}_{-12} per cent of S0s. PAH features (classes 2, 3 and 4), detected in 47^{+8}_{-7} per cent of ETGs, tend to be less frequently found in cluster Es than in their LDE counterparts, suggesting a triggering of the star formation activity in LDEs. ETGs detected in the CO $J = 1$–0 and/or $J = 2$–1 lines
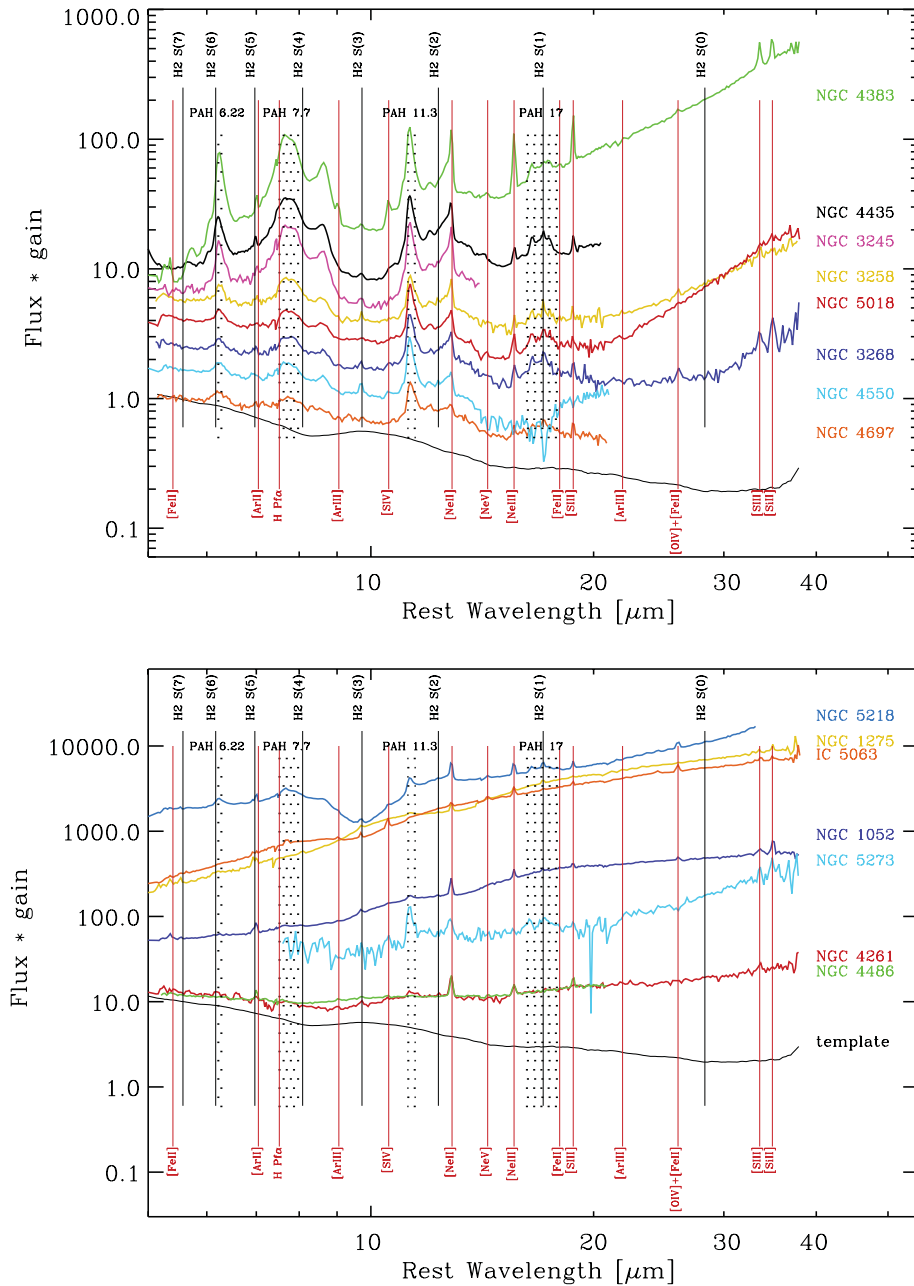
Figure 5. Examples of ETGs with MIR class-3 (top panel) and class-4 (bottom panel) spectra. Fluxes have been normalized to the template and then arbitrarily scaled. PAH features (dotted area) typical of star-forming galaxies together with ionic and/or molecular H_2 emission lines (solid lines) are detected in these spectra. The template passive spectrum is also shown.

Table 6. Demography of MIR spectral classes.

MIR class	E galaxies					S0 galaxies				
	0	1	2	3	4	0	1	2	3	4
Total no. of galaxies	26	7	16	4	3	7	8	12	4	4
No. of galaxies in clusters	10	2	1	0	2	6	3	4	3	0
No. of galaxies in LDE	16	5	15	4	1	1	5	8	1	4

Notes: see text and Tables 1 and 2 for whether galaxies are members of clusters or located in the LDE.

show PAH complexes, with either normal or anomalous ratios, in their MIR nuclear spectra.

(iii) A small fraction (9^{+4}_{-3} per cent) of ETGs show class-3 spectra with normal PAH ratios, typical of star-forming galaxies. The ratio between ETGs with normal (class-3) versus anomalous (class-2) PAHs are produced by a star formation episode with a typical lifetime of 200 Myr. Class-3 ETGs have radio powers typical of star-forming galaxies (Brown et al. 2011).

(iv) The 11.3-μm/7.7-μm PAH ratio is weakly correlated with the galaxy X-ray nuclear luminosity, $L_{X, nuc}$, suggesting a dependence on the radiation field. Class-3 nuclei tend to be less luminous in
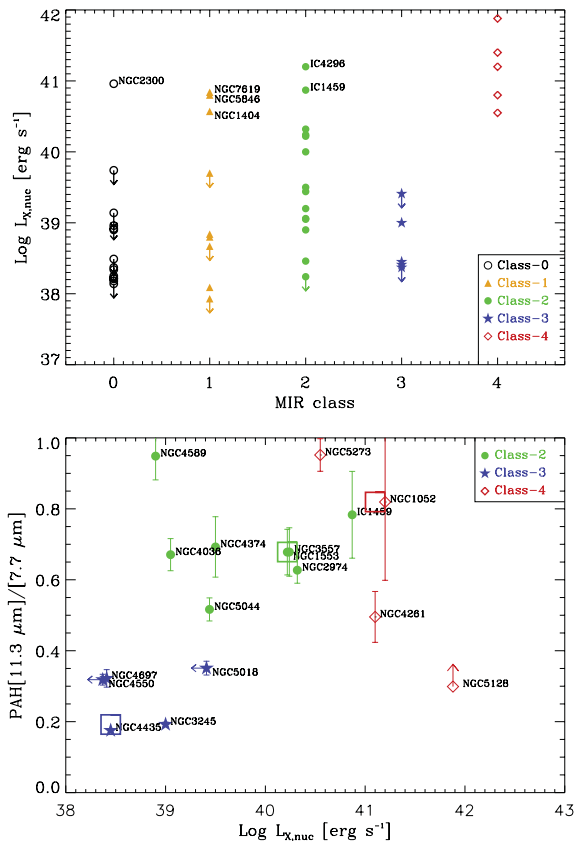
Figure 6. (Top panel) Galaxy nuclear X-ray luminosity, log $L_{X, nuc}$, (Pellegrini 2010) versus MIR class. X-ray-bright galaxies of classes 0, 1, 2 are labelled. (Bottom panel) Ratio of PAH features at 11.3 and 7.7 µm versus log $L_{X, nuc}$. Arrows represent upper limits and are colour-coded as the detections. The large, open squares represent the median values of detected objects in each class. The bottom right diamond refers to the PAH ratio measured for NGC 5128. The strong absorption centred at 10 µm (see Fig. 1) probably perturbs the measure of the PAH line strength so that the PAH ratio is probably a lower limit. Therefore, in addition to the diamond, we label it with an arrow.

the X-ray compared with both class-4 and class-2, where an AGN contribution may be present.

Panuzzo et al. (2011) suggest that each of the five MIR classes is a snapshot of the evolution of ETG nuclei during an accretion episode, starting from, and ending with, a class-0 spectrum. The MIR emission line diagnostic diagram (Dale et al. 2006) is unable to distinguish between the different powering mechanisms ionizing the ISM. MIR classes are successful in identifying those LINER nuclei powered by star formation (class-3). Most ETGs in class-4 indicate the presence of an AGN. Several mechanisms ionizing the ISM seem to be at work, especially in transition class-2, where (low-accretion-rate) AGN, shock-front (X-ray cavities, H_2) and/or past star formation (PAHs) signatures combine. ETGs in class-1 may still show signatures of past activity, for example strong radio emission and X-ray cavities, in some galaxies. The MIR class-1 continuum is indistinguishable from that of class-0, suggesting that this class marks the end of the active phase in the nucleus. Kinematical and/or morphological scars of recent accretion episodes are found in a large fraction (41^{+8}_{-7} per cent) of our ETGs, even in passively evolving galaxies, further supporting the argument for an evolutionary link between the MIR classes and accretion/feedback phenomena.

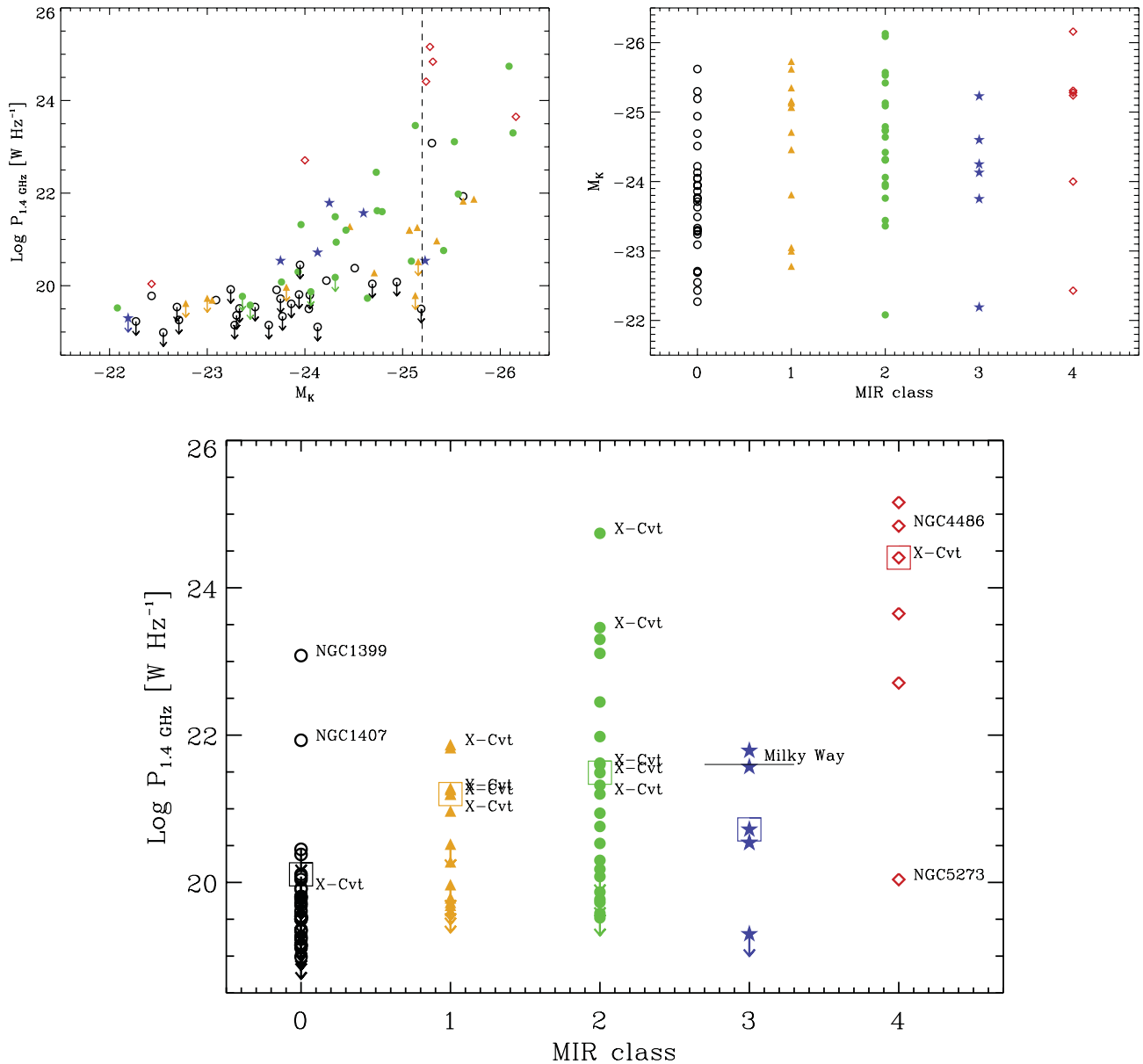**Figure 7.** Emission line diagnostic diagram (from Dale et al. 2006) separating AGNs from LINERs and starburst (SB) ETGs. We indicate MIR classes and have labelled some relevant galaxies.

Figure 8. (Top left) 1.4-GHz radio power versus M_K (open circles, class-0; triangles, class-1; full dots, class-2; stars, class-3; open diamonds, class-4). Arrows represent upper limits. ETGs with $M_K \leq -25.2$, the vertical dashed line, are always detected (see Brown et al. 2011). (Top right) M_K versus MIR class for the radio sample (see Table B1). (Bottom) Radio power versus the MIR class. The radio power of the Milky Way is indicated with a horizontal line (see text). Large open squares represent the median value of the detected objects in each MIR class. ETGs with X-ray-detected cavities (Cavagnolo et al. 2010) are labelled with X-Cvt.

REFERENCES

Allen M. G., Groves B. A., Dopita M. A., Sutherland R. S., Kewley L. J., 2008, ApJS, 178, 20

Annibali F., Bressan A., Rampazzo R., Zeilinger W. W., 2006, A&A, 445, 79

Annibali F., Bressan A., Rampazzo R., Zeilinger W. W., Danese L., 2007, A&A, 463, 455

Annibali F., Bressan A., Rampazzo R., Zeilinger W. W., Vega O., Panuzzo P., 2010, A&A, 519, A40

Armus L. et al., 2007, ApJ, 656, 148

Athey A., Bregman J., Bregman J., Temi P., Sauvage M., 2002, ApJ, 571, 272

Baldwin J. A., Phillips M. M., Terlevich R., 1981, PASP, 93, 5

Bell E. F., 2003, ApJ, 586, 794

Bertola F., Galletta G., Capaccioli M., Rampazzo R., 1988, A&A, 192, 24

Binette L., Magris C. G., Stasińska G., Bruzual A. G., 1994, A&A, 292, 13

Bois M. et al., 2012, MNRAS, 416, 1654

Boroson B., Kim D.-W., Fabbiano G., 2011, ApJ, 729, 12

Brandl B. R. et al., 2006, ApJ, 653, 1129

Bregman J. N., Temi P., Bregman J. D., 2006, ApJ, 647, 265

Bressan A., Granato G. L., Silva L., 1998, A&A, 332, 135

Bressan A. et al., 2006, ApJ, 639, L55

Brown M. J. I., Januzzi B. T., Floyd D. J. E., Mould J. R., 2011, ApJ, 731, L41

Buson L. et al., 2009, ApJ, 705, 356

Capetti A., Balmaverde B., 2006, A&A, 453, 27

Cavagnolo K. W., McNamara B. R., Nulsen P. E. J., Carilli C. L., Jones C., Bîrzan L., 2010, ApJ, 720, 1066

Clemens M. S., Bressan A., Nikolic B., Alexander P., Annibali F., Rampazzo R., 2006, MNRAS, 370, 702

Clemens M. S., Bressan A., Nikolic B., Rampazzo R., 2009, MNRAS, 392, L35

Clemens M. S. et al., 2010, A&A, 518, L50

Coccato L., Corsini E. M., Pizzella A., Morelli L., Funes J. G., Bertola F., 2004, A&A, 416, 507

Corsini E. M., Bertola F., 1998, J. Korean Phys. Soc., 33, 574

Dale D. A. et al., 2006, ApJ, 646, 161

Davies R. L., Efstathiou G., Fall S. M., Illingworth G., Schechter P. L., 1983, ApJ, 266, 41

van Dokkum P. G., 2005, AJ, 130, 2647

van Dokkum P. G., Franx M., 1995, AJ, 110, 2027

Dopita M. A., Sutherland R. S., 1995, ApJ, 455, 468

Draine B. T., Li A., 2007, ApJ, 657, 810

Dupraz C., Combes F., 1986, A&AS, 166, 53

Elson R. A. W., Fall S. M., Freeman K. C., 1987, ApJ, 323, 54

Emsellem E., Cappellari M., Peletier R. F., McDermid R. M., Bacon R., 2004, MNRAS, 352, 721

Eracleous M., Hwang J. A., Flohic H. M. L. G., 2010, ApJ, 711, 796

Fabian A. C., 2012, ARA&A, 50, 455

Feldmann R., Carollo C. M., Mayer L., 2011, ApJ, 736, 88

Ferrari F., Pastoriza M. G., Macchetto F., Caon N., 2002, A&A, 136, 269

Finkelman I., Brosch N., Funes J.-G., Barway S., Kniazev A., Väisänen P., 2012, MNRAS, 422, 1384

Forbes D. A., 1991, MNRAS, 249, 779

Gehrels N., 1986, ApJ, 303, 336

Ghosh K. K., Swartz D. A., Tennant A. F., Wu K., Saripalli L., 2005, ApJ, 623, 815

Gonzàlez-Martín O., Masegosa J., Márquez I., Guainazzi M., Jimènez-Baión E., 2009, A&A, 506, 1107

Goudfrooij P., de Jong T., 1995, A&A, 298, 784

Grützbauch R., Trinchieri G., Rampazzo R., Held E. V., Rizzi L., Sulentic J. W., Zeilinger W. W., 2007, AJ, 133, 220

Heckman T. M., 1980, A&A, 87, 152

Hernquist L., Quinn P., 1987a, ApJ, 312, 1

Henquist L., Quinn P., 1987b, ApJ, 312, 17

Ho L. C., Filippenko A. V., Sargent W. L. W., 1997, ApJ, 487, 568

Kaneda H., Onaka T., Sakon I., 2005, ApJ, 632, L83

Kaneda H., Onaka T., Kitayama T., Okada Y., Sakon I., 2007, PASJ, 59, 107

Kaneda H., Honaka T., Sakon L. I., Kitayama T., Okada Y., Suzuki T., 2008, ApJ, 684, 270

Knapp G. R., Guhathakurta P., Kim D.-W., Jura M. A., 1989, ApJS, 70, 329

Kormendy J., 2004, in Ho L. C., ed., Coevolution of Black Holes and Galaxies, Carnegie Observatories Astrophysics Series. Cambridge Univ. Press, Cambridge, p. 1

Kormendy J., Fisher D. B., Cornell M. E., Bender R., 2009, ApJS, 182, 216

Koski A. T., Osterbrock D. E., 1976, ApJ, 203, L49

Krajnović D. et al., 2008, MNRAS, 390, 93

Lauer T. R. et al., 2005, ApJ, 129, 2138

Longhetti M., Bressan A., Chiosi C., Rampazzo R., 2000, A&A, 353, 917

Lu N. et al., 2003, ApJ, 588, 199

Macchetto F., Pastoriza M., Caon N., Sparks W. B., Giavalisco M., Bender R., Capaccioli M., 1996, A&A, 120, 463

Machacek M. E., Jones C., Forman W. R., 2004, ApJ, 610, 813

Malin D. F., Carter D., 1983, ApJ, 274, 534

Maoz D., Nagar N. M., Falcke H., Wilson A. S., 2005, ApJ, 625, 699

Marigo P., Girardi L., 2007, A&A, 469, 239

Marino A. et al., 2011, MNRAS, 411, 311

Moore B., Katz N., Lake G., Dressler A., Oemler A., 1996, Nat, 379, 613

Morganti R., 2010, PASA, 27, 463

Morganti R., Holt J., Saripalli L., Oosterloo T. A., Tadhunter C. N., 2007, A&A, 476, 735

Morganti R., Frieswijk W., Oonk R. J. B., Oosterloo T., Tadhunter C., 2013, A&A, 552, L4

Ocaña Flaquer B., Combes F., Leon S., Lim J., 2010, A&A, 518, A9

Ogle P., Antonucci R., Appleton P. N., Whysong D., 2007, ApJ, 668, 699

Panuzzo P. et al., 2007, ApJ, 656, 206

Panuzzo P., Rampazzo R., Bressan A., Vega O., Annibali F., Buson L. M., Clemens M. S., Zeilinger W. W., 2011, A&A, 528, A10

Patil M. K., Pandey S. K., Sahu D. K., Kembhavi A., 2007, A&A, 461, 103

Pellegrini S., 2005, ApJ, 624, 155

Pellegrini S., 2010, ApJ, 717, 640

Phillips M. M., Jenkins C. R., Dopita M. A., Sadler E. M., Binette L., 1986, AJ, 91, 1062

Pian E., Romano P., Maoz D., Cucchiara A., Pagani C., Parola V. L., 2010, MNRAS, 401, 677

Pierfederici F., Rampazzo R., 2004, Astron. Nachr., 325, 359

Pinkney J. et al., 2003, ApJ, 596, 903

Pu S. B., Saglia R. P., Fabricius M. H., Thomas J., Bender R., Han Z., 2010, A&A, 516, 4

Rampazzo R., 1988, A&A, 204, 81

Rampazzo R., Annibali F., Bressan A., Longhetti M., Padoan F., Zeilinger W. W., 2005, A&A, 433, 497

Rampazzo R. et al., 2011, Ap&SS, 335, 201

Roussel H. et al., 2007, ApJ, 669, 659

Sadler E. M., Gerhard O. E., 1995, MNRAS, 1985, 2141985, 214, 177

Salomé P. et al., 2006, A&A, 454, 437

Sandage A., Tammann G. A., 1987, A revised Shapley-Ames Catalog of bright galaxies. Carnegie Institution of Washington Publication.2nd edn, Carnegie Intistution, Washington

Sargsyan L., Weedman D., Lebouteiller V., Houck J., Barry D., Hovhannisyan A., Mickaelian A., 2011, ApJ, 730, 19

Sarzi M. et al., 2006, MNRAS, 366, 1151

Sarzi M. et al., 2010, MNRAS, 402, 2187

Serra P., Trager S. C., Oosterloo T. A., Morganti R., 2008, A&A, 483, 57

Shankahr F., Salucci P., Danese L., 2004, in Dettmar R., Klein U., Salucci P., eds, Proc. Science, Baryons in Dark Matter Haloes. SISSA, p. 59.1, available at: http://pos.sissa.it/cgi-bin/reader/conf.cgi?confid=14

Sil'chenko O. K., Moiseev A. V., Afanasiev V. L., 2009, ApJ, 694, 1550

Simões L., Ramiro D., Storchi-Bergmann T., de Fátima S. M., Martini P., 2007, ApJ, 655, 718

Smith J. D. T. et al., 2007, ApJ, 656, 770

Smolcić V., Rieckers D. A., 2011, ApJ, 730, 64

Sofue Y., Wakamatsu K., 1993, PASJ, 45, 529

Stasińska G., Vale Asari N., Cid Fernandes R., Gomes J. M., Schlickmann M., Mateus A., Schoenell W., Sodré L. Jr, 2008, MNRAS, 391, L29

Tal T., van Dokkum P. G., Nelan J., Bezanson R., 2009, AJ, 138, 1417

Temi P., Brighenti F., Mathews W. G., 2007, ApJ, 666, 222

Thomson R. C., 1991, MNRAS, 253, 256

Thomson R. C., Wright A. E., 1990, MNRAS, 224, 895

Thronson H. A., Tacconi L., Kenney J., Greenhouse M. A., Margulis M., Tacconi-Garman L., Young J. S., 1989, ApJ, 344, 747

Tremblay G. R., Chiaberge M., Donzelli C. J., Quillen A. C., Capetti A., Sparks W. B., Macchetto F. D., 2007, ApJ, 666, 109

Trinchieri G., di Serego Alighieri S., 1991, AJ, 101, 1647

Trinchieri G., Goudfrooij P., 2002, A&A, 386, 472

Tully R. B., 1988, Nearby Galaxies Catalog. Cambridge Univ. Press, Cambridge

Tully R. B., Rizzi L., Shaya E. J., Courtois H. M., Makarov D. I., Jacobs B. A., 2009, AJ, 138, 323

Van Verlzen S., Falcke H., Schellart P., Nierstenhöfer N., Kampert K.-H., 2012, A&A, in press

de Vaucouleurs G., de Vaucouleurs A., Corwin H. G. Jr., Buta R. J., Paturel G., Fouqué P., 1991, Third Reference Catalogue of Bright Galaxies. Springer-Verlag, New York

Vega O. et al., 2010, ApJ, 721, 1090

Verhoelst T., van der Zypen N., Hony S., Decin L., Cami J., Eriksson K., 2009, A&A, 498, 127

Véron-Cetty M.-P., Véron P., 1988, A&A, 204, 28

Wall J. V., 1977, Unpublished lecture notes, Mullard Radio Astronomy Observatory, Cavendish Laboratory, Cambridge

Welch G. A., Sage L. J., Young L. M., 2010, ApJ, 725, 100

Whitmore B. C., Lucas R. A., McElroy D. B., Steiman-Cameron T. Y., Sackett P. D., Olling R. P., 1990, AJ, 100, 1489

Wiklind T., Henkel C., 2001, A&A, 375, 797

Wrobel J. M., Heeshen D. S., 1988, ApJ, 335, 677

Yan R., Newman J. A., Faber S. M., Konidaris N., Koo D., Davis M., 2006, ApJ, 648, 281

Young L. M. et al., 2011, MNRAS, 414, 940

Zhang Y., Gu Q.-S., Ho L. C., 2008, A&A, 487, 177

APPENDIX A: INTENSITIES OF PAH COMPLEXES AND NEBULAR AND MOLECULAR EMISSIONS

Table A1 lists the intensity of PAH complexes of ETGs in the MIR spectral classes 2, 3 and 4. Table A2 lists the intensity of nebular

and molecular line emission of ETGs in the MIR spectral classes 1, 2, 3 and 4. See Section 4 for details.

APPENDIX B: TABLES OF NUCLEAR PROPERTIES OF ETGS

We collect in Appendix a set of tables summarizing the properties of ETGs used to characterize the MIR spectral classes in the atlas. References are reported in the legend of each table.

In Table B1 we report the optical 'activity' class (columns 3 and 8), the nuclear (2-arcsec radius) X-ray luminosity, $L_{X, nuc}$ (columns

Table A1. PAH complex intensities.

Galaxy	6.22 μm (10^{-18} W m^{-2})	7.7 μm[a] (10^{-18} W m^{-2})	8.6 μm (10^{-18} W m^{-2})	11.3 μm[b] (10^{-18} W m^{-2})	12.7 μm[c] (10^{-18} W m^{-2})	17 μm[d] (10^{-18} W m^{-2})
E						
NGC 1275	–	1047.2 ± 226.2	–	439.2 ± 141.9	794.2 ± 250.7	–
NGC 1297	13.3 ± 4.4	62.9 ± 3.3	13.8 ± 1.0	44.9 ± 1.4	21.8 ± 1.3	23.6 ± 2.5
NGC 1395	–	–	–	39.6 ± 3.4	27.6 ± 3.4	–
NGC 1453	–	77.4 ± 10.7	10.6 ± 2.4	31.0 ± 2.8	20.8 ± 2.1	13.2 ± 1.7
NGC 1549	–	–	–	9.6 ± 3.0	–	4.1 ± 1.1
NGC 2974	88.3 ± 9.4	409.7 ± 21.1	44.0 ± 3.9	256.9 ± 7.2	113.5 ± 5.7	144.9 ± 5.3
NGC 3258	113.8 ± 4.9	537.6 ± 15.3	110.4 ± 4.6	119.4 ± 3.1	72.0 ± 2.9	44.1 ± 1.4
NGC 3268	67.5 ± 6.4	341.1 ± 9.6	48.3 ± 2.9	150.5 ± 4.3	83.6 ± 4.1	73.3 ± 2.5
NGC 3557	32.5 ± 10.7	134.9 ± 11.5	19.6 ± 5.8	91.5 ± 4.9	48.4 ± 5.8	32.5 ± 3.9
NGC 3962	31.9 ± 8.8	133.1 ± 8.8	24.6 ± 3.8	102.8 ± 4.6	37.3 ± 2.9	35.3 ± 4.8
NGC 4261	40.4 ± 8.6	117.3 ± 13.8	11.6 ± 2.7	58.1 ± 4.9	53.6 ± 4.3	7.4 ± 1.3
NGC 4374	65.7 ± 20.6	258.3 ± 28.7	51.3 ± 6.6	178.9 ± 9.4	95.1 ± 7.0	65.2 ± 4.7
NGC 4486	–	89.6 ± 26.1	–	–	30.2 ± 9.7	–
NGC 4589	13.9 ± 4.2	52.5 ± 3.4	21.1 ± 1.1	49.8 ± 1.4	21.6 ± 2.1	27.7 ± 1.1
NGC 4696	–	–	–	11.3 ± 1.7	–	7.5 ± 0.5
NGC 4697	211.0 ± 21.2	816.8 ± 44.5	199.0 ± 16.2	263.0 ± 14.2	179.3 ± 5.0	78.4 ± 7.9
NGC 5018	232.1 ± 13.8	938.9 ± 39.4	233.7 ± 13.1	329.5 ± 11.9	152.1 ± 6.1	133.8 ± 7.1
NGC 5044	29.4 ± 7.0	112.5 ± 5.8	32.1 ± 3.1	58.1 ± 2.1	27.1 ± 1.8	28.8 ± 0.9
NGC 5077	–	66.6 ± 6.5	22.3 ± 4.7	30.8 ± 2.5	14.0 ± 1.8	41.2 ± 2.6
NGC 5090	13.5 ± 4.1	80.6 ± 13.4	10.5 ± 1.6	34.5 ± 2.4	21.8 ± 2.4	11.7 ± 3.1
IC 1459	–	108.4 ± 15.1	6.1 ± 1.8	84.9 ± 6.0	41.0 ± 5.4	47.1 ± 4.7
IC 3370	–	62.9 ± 19.6	13.1 ± 3.5	22.2 ± 3.6	22.5 ± 5.7	21.5 ± 2.5
IC 4296	–	–	–	26.7 ± 5.8	26.0 ± 5.6	19.8 ± 5.6
E/S0						
NGC 1052	120.0 ± 33.0	239.0 ± 41.4	–	195.8 ± 40.4	–	254.1 ± 66.3
NGC 4550	59.9 ± 5.3	323.2 ± 12.0	79.7 ± 5.1	102.9 ± 3.1	33.1 ± 2.1	–
NGC 4636	–	–	–	20.7 ± 5.0	–	8.8 ± 0.8
NGC 5353	–	52.5 ± 11.9	5.12 ± 1.1	27.4 ± 1.5	15.7 ± 1.2	13.9 ± 1.1
NGC 6868	50.5 ± 12.3	241.7 ± 24.3	27.5 ± 2.9	129.6 ± 6.9	86.8 ± 4.9	45.6 ± 3.1
S0						
NGC 1533	–	–	–	31.3 ± 3.8	12.6 ± 2.1	27.4 ± 1.9
NGC 1553	105.6 ± 10.3	406.8 ± 35.3	48.7 ± 7.4	275.8 ± 10.5	84.4 ± 7.0	78.3 ± 5.5
NGC 2685	–	128.9 ± 10.7	12.6 ± 1.4	85.6 ± 3.2	44.1 ± 3.1	41.6 ± 2.1
NGC 3245	1242.0 ± 47.1	4490.2 ± 85.2	567.7 ± 19.7	863.9 ± 23.3	439.4 ± 24.1	–
NGC 4036	106.4 ± 15.6	194.1 ± 11.6	42.9 ± 5.3	130.2 ± 4.1	75.9 ± 4.1	–
NGC 4371	–	55.2 ± 7.8	30.7 ± 7.2	21.3 ± 2.5	8.1 ± 1.5	5.1 ± 1.1
NGC 4383	3691.8 ± 81.7	12597.3 ± 158.3	2985.3 ± 72.8	2710.8 ± 65.4	1486.1 ± 38.1	563.2 ± 56.9
NGC 4435	1304.5 ± 29.1	5906.7 ± 86.7	805.1 ± 21.5	1035.7 ± 23.7	802.2 ± 31.8	357.6 ± 15.3
NGC 4477	104.4 ± 14	278.6 ± 12.6	25.6 ± 1.9	133.7 ± 4.1	59.3 ± 2.8	64.7 ± 2.1
NGC 4552	–	–	–	38.3 ± 7.9	–	7.9 ± 1.8
NGC 5128	3337.4 ± 295.6	18734.1 ± 909.5	>1569.1 ± 330.6	>5603.1 ± 511.2	4251.8 ± 715.7	5230.6 ± 461.3
NGC 5273	–	346.2 ± 12.9	279.1 ± 15.1	329.5 ± 10.1	97.4 ± 5.5	320.6 ± 16.1
NGC 5631	–	87.3 ± 3.4	31 ± 1.1	45.5 ± 2.1	21.8 ± 2.1	28.9 ± 2.1
NGC 5898	–	53 ± 16.3	–	46.5 ± 4.3	15.1 ± 3.3	21.7 ± 2.4
IC 5063	–	1190.4 ± 140.9	208.8 ± 68.9	462.9 ± 125.4	–	–

Notes. Uncertainties are 1σ. [a] Includes the 7.42-, 7.60- and the 7.85-μm features. [b] Includes the 11.23- and the 11.33-μm features. [c] Includes the 12.62- and the 12.69-μm features. [d] Includes the 16.45-, 17.04-, 17.375- and the 17.87-μm features. We consider the 8.6- and 11.3-μm PAH emissions in NGC 5128 as lower limits because of the huge silicate absorption.

Table A2. Nebular and molecular emission line intensities.

Galaxy	H$_2$ 0–0 S(7) 5.51 μm	H$_2$ 0–0 S(6) 6.11 μm	H$_2$ 0–0 S(5) 6.91 μm	[ArII] 6.99 μm	H Pfα 7.46 μm	H$_2$ 0–0 S(4) 8.03 μm	[Ar III] 8.99 μm	H$_2$ 0–0 S(3) 9.66 μm	[S IV] 10.51 μm	H$_2$ 0–0 S(2) 12.28 μm
E										
NGC 1209	–	–	–	4.8 ± 1.0	–	–	3.5 ± 0.9	–	–	1.4 ± 0.2
NGC 1275	120.4 ± 31.9	–	194.4 ± 25.0	128.7 ± 18.4	–	–	–	184.9 ± 35.5	–	–
NGC 1297	–	–	2.8 ± 0.3	3.3 ± 0.3	–	0.5 ± 0.1	1.2 ± 0.3	5.1 ± 0.5	0.6 ± 0.2	2.1 ± 0.1
NGC 1395	–	–	–	–	–	–	–	–	–	1.8 ± 0.4
NGC 1404	–	–	–	–	–	–	–	–	–	–
NGC 1453	–	8.5 ± 1.7	–	9.0 ± 1.1	3.9 ± 0.6	–	–	7.1 ± 1.7	2.2 ± 1.0	1.1 ± 0.2
NGC 1549	–	–	–	–	–	–	–	–	–	–
NGC 1700	–	–	–	–	–	–	–	–	–	–
NGC 2974	9.0 ± 2.5	3.8 ± 0.5	16.1 ± 0.8	18.7 ± 1.4	–	4.2 ± 0.3	–	30.9 ± 1.7	4.1 ± 0.6	13.3 ± 0.8
NGC 3258	–	–	4.1 ± 0.3	8.5 ± 0.5	–	2.3 ± 0.1	0.8 ± 0.1	5.1 ± 0.8	0.7 ± 0.2	4.2 ± 0.2
NGC 3268	–	–	6.1 ± 0.6	7.7 ± 0.5	–	1.6 ± 0.1	0.5 ± 0.1	4.5 ± 0.7	1.6 ± 0.3	2.4 ± 0.2
NGC 3557	–	–	–	5.4 ± 0.6	–	–	–	–	–	–
NGC 3962	–	–	3.1 ± 0.7	8.6 ± 1.0	–	4.5 ± 0.4	2.5 ± 0.7	16.6 ± 1.5	2.2 ± 0.6	4.8 ± 0.3
NGC 4261	–	–	6.6 ± 1.1	12.4 ± 1.3	–	–	3.3 ± 1.1	5.2 ± 1.7	4.2 ± 1.0	5.3 ± 0.4
NGC 4374	–	–	7.4 ± 1.0	24.4 ± 2.2	–	1.3 ± 0.1	6.9 ± 1.5	8.3 ± 2.0	5.2 ± 1.2	3.6 ± 0.5
NGC 4486	–	–	–	36.0 ± 3.0	–	–	8.2 ± 2.6	–	–	–
NGC 4589	1.4 ± 0.4	–	–	1.1 ± 0.3	–	–	1.0 ± 0.3	–	–	–
NGC 4696	–	–	3.5 ± 0.8	8.4 ± 0.9	–	–	–	6.4 ± 0.9	–	1.5 ± 0.1
NGC 4697	14.5 ± 3.2	8.2 ± 1.1	7.4 ± 1.2	12.9 ± 1.1	0.3 ± 0.1	6.4 ± 0.5	8.2 ± 1.2	8.2 ± 2.0	–	1.6 ± 0.1
NGC 5011	–	–	–	7.2 ± 1.0	–	–	2.1 ± 0.6	3.6 ± 0.6	1.8 ± 0.5	–
NGC 5018	–	6.3 ± 1.0	7.5 ± 1.0	9.6 ± 1.0	–	4.3 ± 0.4	3.4 ± 0.5	4.9 ± 1.6	–	4.7 ± 0.5
NGC 5044	6.4 ± 1.3	1.8 ± 0.4	14.9 ± 0.9	14.6 ± 0.5	–	2.9 ± 0.2	1.8 ± 0.3	23.4 ± 1.1	1.2 ± 0.3	10.6 ± 0.4
NGC 5077	–	–	6.2 ± 1.1	9.1 ± 0.8	3.5 ± 0.6	1.7 ± 0.2	2.6 ± 0.6	9.4 ± 0.9	1.2 ± 0.5	2.8 ± 0.4
NGC 5090	–	3.5 ± 0.9	7.0 ± 0.6	9.2 ± 0.8	–	1.8 ± 0.2	3.0 ± 0.8	–	3.1 ± 0.5	–
NGC 5813	–	7.5 ± 1.5	6.4 ± 0.6	15.3 ± 1.3	–	2.9 ± 0.4	3.6 ± 1.0	6.3 ± 0.9	–	–
NGC 7619	–	–	–	–	–	–	–	–	–	–
IC 1459	–	–	5.0 ± 1.6	21.2 ± 1.5	–	–	–	10.3 ± 2.4	–	2.6 ± 0.5
IC 2006	–	–	–	–	–	–	–	–	–	–
IC 3370	–	–	4.2 ± 0.3	4.8 ± 0.4	–	–	2.3 ± 0.3	3.7 ± 0.4	–	2.2 ± 0.2
IC 4296	–	–	–	–	–	–	–	–	–	2.2 ± 0.5
E/S0										
NGC 1052	17.8 ± 3.1	8.7 ± 2.7	31.5 ± 7.8	81.0 ± 2.7	–	6.7 ± 2.0	17.0 ± 2.9	63.3 ± 10.7	–	11.2 ± 3.9
NGC 4472	–	–	3.1 ± 1.0	11.3 ± 2.5	–	–	–	–	–	–
NGC 4550	–	2.0 ± 0.4	3.4 ± 0.4	2.7 ± 0.3	–	–	1.3 ± 0.2	6.4 ± 0.6	1.9 ± 0.4	2.4 ± 0.3
NGC 4636	–	–	–	–	–	–	–	–	–	–
NGC 5353	–	–	–	–	–	–	–	2.0 ± 0.6	–	1.1 ± 0.1
NGC 6868	7.0 ± 2.0	3.5 ± 1.0	20.2 ± 1.4	16.3 ± 1.0	–	6.0 ± 0.5	4.0 ± 0.6	23.9 ± 1.5	1.4 ± 0.4	8.9 ± 0.3
S0										
NGC 584	–	–	–	–	–	–	–	–	–	–
NGC 1366	–	–	–	–	–	–	–	–	–	–
NGC 1533	–	–	–	2.2 ± 0.5	3.8 ± 1.2	–	–	3.6 ± 0.7	–	1.8 ± 0.4
NGC 1553	–	1.5 ± 0.3	5.9 ± 0.8	10.6 ± 1.2	–	3.7 ± 0.4	–	10.8 ± 2.7	3.7 ± 0.8	6.2 ± 0.6
NGC 2685	–	–	–	7.6 ± 1.0	2.3 ± 0.6	2.4 ± 0.3	4.2 ± 0.9	7.9 ± 1.0	3.0 ± 0.6	2.7 ± 0.3
NGC 3245	–	–	25.0 ± 1.5	36.8 ± 1.8	18.1 ± 8.0	–	–	–	–	–
NGC 4036	–	24.6 ± 3.0	20.5 ± 1.2	7.5 ± 1.1	–	10.6 ± 1.0	8.8 ± 1.2	35.7 ± 2.1	1.5 ± 0.4	13.8 ± 1.0
NGC 4371	–	–	–	–	–	–	–	–	–	1.2 ± 0.3
NGC 4382	–	–	–	–	–	–	–	–	–	–
NGC 4383	–	–	–	91.3 ± 5.0	–	–	83.1 ± 3.1	–	81.3 ± 17.2	–
NGC 4435	–	–	25.0 ± 1.5	40.0 ± 2.0	–	22.2 ± 2.0	–	–	–	–
NGC 4477	–	4.0 ± 1.0	9.0 ± 1.0	18.9 ± 1.3	–	3.2 ± 0.4	4.9 ± 0.7	12.8 ± 1.7	2.9 ± 0.7	7.0 ± 0.5
NGC 4552	–	–	–	–	–	–	–	10.4 ± 3.4	–	2.8 ± 0.9
NGC 4649	–	–	–	–	–	–	–	–	–	–
NGC 5128	–	83.4 ± 22.2	246.6 ± 40.2	804.3 ± 92.9	–	54.5 ± 8.9	82.9 ± 26.2	231.7 ± 71.3	–	213.7 ± 69.3
NGC 5273	–	–	–	–	–	22.9 ± 2.0	–	–	30.4 ± 8.0	9.5 ± 0.8
NGC 5631	–	–	6.3 ± 1.3	3.8 ± 1.0	5.9 ± 1.2	–	3.4 ± 1.1	11.0 ± 1.5	–	–
NGC 5846	–	–	–	–	–	–	–	0.5 ± 0.1	–	0.6 ± 0.1
NGC 5898	–	–	–	–	–	–	–	4.1 ± 1.4	–	0.9 ± 0.2
NGC 7192	–	–	–	2.6 ± 0.8	–	–	–	–	–	–
NGC 7332	–	–	–	–	–	–	–	3.9 ± 0.2	–	–
IC 5063	–	–	133.8 ± 27.7	106.5 ± 29.6	–	–	176.3 ± 44.8	244.9 ± 49.9	788.5 ± 123.9	–

Table A2 – *continued*

Galaxy	[Ne ɪɪ] 12.81 μm	[Ne ᴠ] 14.32 μm	[Ne ɪɪɪ] 15.55 μm	H₂ 0–0 S(1) 17.03 μm	[Fe ɪɪ] 17.94 μm	[S ɪɪɪ] 18.71 μm	[Ar ɪɪɪ] 21.83 μm	[Ne ᴠ] 24.32 μm	[O ɪᴠ][d] 25.89 μm	[Fe ɪɪ][d] 25.99 μm
E										
NGC 1209	3.1 ± 0.3	–	3.0 ± 0.2	–	0.9 ± 0.1	1.5 ± 0.1	–	–	0.4 ± 0.1	2.1 ± 0.2
NGC 1275	507.1 ± 50.1	–	398.6 ± 98.8	–	–	–	–	–	–	–
NGC 1297	1.9 ± 0.1	–	1.2 ± 0.1	7.5 ± 0.2	–	0.4 ± 0.1	–	–	0.8 ± 0.1	1.0 ± 0.1
NGC 1395	2.8 ± 0.2	–	–	–	–	–	–	–	–	–
NGC 1404	5.9 ± 2.0	–	4.3 ± 1.5	–	–	–	–	–	–	–
NGC 1453	3.6 ± 0.4	–	7.5 ± 0.5	2.2 ± 0.2	–	2.3 ± 0.3	–	–	–	–
NGC 1549	2.5 ± 0.4	–	4.4 ± 0.5	0.8 ± 0.2	–	1.6 ± 0.4	–	–	–	–
NGC 1700	–	–	2.8 ± 0.9	–	–	–	–	–	–	–
NGC 2974	35.0 ± 1.0	–	27.5 ± 1.2	21.8 ± 1.1	–	13.3 ± 0.9	–	7.3 ± 0.9	2.1 ± 0.2	10.3 ± 0.6
NGC 3258	15.2 ± 0.5	–	4.6 ± 0.3	6.6 ± 0.3	1.2 ± 0.2	3.7 ± 0.3	2.2 ± 0.5	–	1.1 ± 0.2	1.8 ± 0.4
NGC 3268	10.5 ± 0.4	–	5.5 ± 0.2	3.0 ± 0.3	1.0 ± 0.3	3.4 ± 0.2	1.3 ± 0.2	–	1.0 ± 0.1	1.9 ± 0.2
NGC 3557	9.6 ± 0.6	–	9.0 ± 0.6	–	1.4 ± 0.2	2.7 ± 0.3	–	1.1 ± 0.3	0.8 ± 0.1	2.8 ± 0.3
NGC 3962	14.2 ± 0.4	1.0 ± 0.1	8.2 ± 0.5	4.7 ± 0.2	2.8 ± 0.2	5.3 ± 0.2	–	–	3.1 ± 0.2	3.0 ± 0.2
NGC 4261	31.7 ± 1.6	1.7 ± 0.4	11.6 ± 0.8	–	–	1.3 ± 0.3	–	–	–	–
NGC 4374	32.9 ± 1.3	1.6 ± 0.3	26.5 ± 1.1	8.3 ± 0.6	1.7 ± 0.3	14.9 ± 0.5	2.5 ± 0.6	–	3.5 ± 0.3	5.7 ± 0.6
NGC 4486	58.3 ± 2.8	–	24.1 ± 2.7	–	–	19.1 ± 3.1	–	–	–	–
NGC 4589	0.4 ± 0.1	–	0.3 ± 0.1	0.3 ± 0.1	–	0.3 ± 0.1	–	–	–	–
NGC 4696	13.3 ± 0.6	–	7.6 ± 0.3	6.4 ± 0.3	–	1.2 ± 0.1	–	–	1.5 ± 0.1	2.8 ± 0.2
NGC 4697	8.3 ± 0.6	–	9.1 ± 1.1	4.0 ± 0.5	–	5.8 ± 0.8	–	–	–	–
NGC 5011	2.8 ± 0.3	0.6 ± 0.2	3.9 ± 0.3	–	–	1.8 ± 0.1	–	–	0.9 ± 0.1	0.5 ± 0.1
NGC 5018	19.7 ± 1.0	–	15.9 ± 1.0	7.3 ± 0.4	–	6.0 ± 0.7	–	–	2.5 ± 0.4	3.1 ± 0.7
NGC 5044	24.3 ± 0.9	–	12.2 ± 0.4	13.4 ± 0.5	0.6 ± 0.1	3.1 ± 0.2	1.0 ± 0.2	1.2 ± 0.2	1.5 ± 0.1	2.1 ± 0.2
NGC 5077	20.6 ± 1.0	0.6 ± 0.1	17.9 ± 0.8	12.7 ± 0.7	1.4 ± 0.2	6.3 ± 0.4	2.9 ± 0.6	–	1.7 ± 0.1	8.4 ± 0.5
NGC 5090	20.7 ± 0.6	0.9 ± 0.1	9.4 ± 0.6	1.6 ± 0.3	3.8 ± 0.4	4.0 ± 0.3	4.1 ± 0.4	–	2.7 ± 0.3	2.2 ± 0.2
NGC 5813	6.3 ± 0.3	–	7.0 ± 0.3	2.3 ± 0.4	–	3.0 ± 0.2	–	–	–	–
NGC 7619	–	–	1.4 ± 0.6	–	–	–	–	–	–	–
IC 1459	51.4 ± 2.1	–	38.7 ± 1.7	1.4 ± 0.3	3.6 ± 0.6	9.9 ± 0.7	–	4.7 ± 1.1	2.8 ± 0.3	12.3 ± 1.0
IC 2006	–	–	3.4 ± 1.6	–	–	–	–	–	–	–
IC 3370	2.1 ± 0.1	–	1.4 ± 0.1	4.4 ± 0.2	–	0.6 ± 0.1	–	0.3 ± 0.1	0.7 ± 0.1	0.9 ± 0.1
IC 4296	24.1 ± 1.4	0.5 ± 0.1	10.9 ± 0.7	1.7 ± 0.5	1.4 ± 0.3	4.2 ± 0.6	–	–	3.9 ± 0.4	2.9 ± 0.2
E/S0										
NGC 1052	250.3 ± 9.7	–	180.4 ± 9.3	47.5 ± 9.7	43.6 ± 12.6	71.4 ± 9.4	–	–	27.2 ± 3.9	50.1 ± 9.3
NGC 4472	2.7 ± 0.7	–	–	–	–	–	–	–	–	–
NGC 4550	4.3 ± 0.3	–	–	–	–	–	–	–	–	–
NGC 4636	12.9 ± 0.8	–	15.1 ± 0.8	2.4 ± 0.4	–	6.1 ± 0.5	–	–	–	–
NGC 5353	2.5 ± 0.2	–	3.3 ± 0.3	2.1 ± 0.1	–	1.7 ± 0.2	–	–	0.7 ± 0.1	1.8 ± 0.2
NGC 6868	30.0 ± 1.0	1.1 ± 0.1	23.8 ± 0.8	9.6 ± 0.6	1.5 ± 0.2	7.8 ± 0.4	1.3 ± 0.4	2.0 ± 0.4	4.8 ± 0.3	6.6 ± 0.4
S0										
NGC 584	3.1 ± 1.0	–	6.5 ± 0.7	–	–	–	–	–	–	–
NGC 1366	1.9 ± 0.4	–	3.4 ± 0.4	–	–	1.7 ± 0.2	–	–	0.5 ± 0.1	0.5 ± 0.1
NGC 1533	5.3 ± 0.3	–	6.6 ± 0.4	4.5 ± 0.2	–	5.7 ± 0.4	1.6 ± 0.2	–	0.6 ± 0.1	3.0 ± 0.3
NGC 1553	25.1 ± 0.9	0.4 ± 0.1	22.3 ± 1.6	5.7 ± 0.5	–	8.5 ± 0.9	–	–	1.3 ± 0.2	6.1 ± 0.9
NGC 2685	8.6 ± 0.5	–	6.9 ± 0.4	5.2 ± 0.3	–	0.5 ± 0.1	–	–	1.4 ± 0.2	2.4 ± 0.2
NGC 3245	104.6 ± 13.6	–	–	–	–	–	–	–	–	–
NGC 4036	34.2 ± 1.4	–	–	–	–	–	–	–	–	–
NGC 4371	1.8 ± 0.2	–	0.7 ± 0.2	–	–	–	–	–	–	–
NGC 4382	–	–	3.4 ± 0.9	–	–	–	–	–	–	–
NGC 4383	359 ± 11.1	–	373.0 ± 16.3	24.6 ± 8.0	–	305.5 ± 19.3	–	–	26.9 ± 7.6	25.6 ± 8.0
NGC 4435	85.9 ± 2.3	–	22.2 ± 2.6	17.6 ± 2.2	–	22.4 ± 1.7	–	–	–	–
NGC 4477	20.2 ± 1.0	1.1 ± 0.3	19.7 ± 1.0	12.8 ± 0.6	1.5 ± 0.2	9.3 ± 0.4	–	–	4.5 ± 0.4	5.6 ± 0.4
NGC 4552	13.5 ± 1.1	0.3 ± 0.1	10.4 ± 1.1	–	–	10.0 ± 1.0	–	–	–	–
NGC 4649	2.2 ± 0.8	–	3.7 ± 0.8	–	–	–	–	–	–	–
NGC 5128	2057.8 ± 118.1	201.4 ± 64.2	1297.1 ± 148.6	634.7 ± 60.2	–	710.9 ± 62.2	–	–	541.3 ± 75.3	551.3 ± 109.2
NGC 5273	27.0 ± 1.3	–	16.4 ± 1.6	7.5 ± 1.2	–	9.7 ± 1.5	–	–	–	–
NGC 5631	3.4 ± 0.1	–	3.2 ± 0.1	4.6 ± 0.2	–	1.0 ± 0.1	–	2.4 ± 0.2	1.4 ± 0.1	1.7 ± 0.1
NGC 5846	12.5 ± 0.9	–	9.1 ± 0.6	2.0 ± 0.2	–	3.8 ± 0.3	–	–	–	–
NGC 5898	4.2 ± 0.3	–	8.3 ± 0.5	3.1 ± 0.3	–	3.8 ± 0.4	–	1.2 ± 0.4	0.5 ± 0.1	2.1 ± 0.2
NGC 7192	2.4 ± 0.4	–	1.0 ± 0.2	0.3 ± 0.1	0.3 ± 0.1	0.3 ± 0.1	1.0 ± 0.2	–	–	0.6 ± 0.1
NGC 7332	–	–	9.0 ± 0.9	1.7 ± 0.3	–	3.4 ± 0.5	–	1.2 ± 0.4	3.4 ± 0.2	4.7 ± 0.3
IC 5063	238.7 ± 48.2	335.2 ± 68.7	1103.6 ± 88.9	168.1 ± 36.9	–	321.7 ± 71.2	–	402.8 ± 107.1	477.1 ± 44.8	673.0 ± 51.4

Table A2 – *continued*

Galaxy	H$_2$ 0–0 S(0) 28.22 μm	[S III] 33.48 μm	[Si II] 34.82 μm	[Fe II] 35.35 μm	[Ne III] 36.01 μm
E					
NGC 1209	–	3.5 ± 0.2	11.3 ± 0.3	–	1.1 ± 0.1
NGC 1275	–	456.0 ± 122.0	847.4 ± 127.8	–	–
NGC 1297	3.0 ± 0.1	1.5 ± 0.1	5.5 ± 0.2	0.3 ± 0.1	–
NGC 1395	–	–	–	–	–
NGC 1404	–	–	–	–	–
NGC 1453	–	–	–	–	–
NGC 1549	–	–	–	–	–
NGC 1700	–	–	–	–	–
NGC 2974	2.6 ± 0.6	13.5 ± 1.2	44.9 ± 1.2	–	–
NGC 3258	–	5.6 ± 0.5	–	–	–
NGC 3268	–	4.8 ± 0.3	7.6 ± 0.5	–	–
NGC 3557	–	8.4 ± 0.4	7.1 ± 0.4	2.7 ± 0.3	4.3 ± 0.3
NGC 3962	–	6.2 ± 0.5	31.7 ± 1.0	1.4 ± 0.4	2.1 ± 0.3
NGC 4261	2.7 ± 0.9	9.3 ± 1.1	–	–	–
NGC 4374	2.2 ± 0.6	24.3 ± 1.0	40.8 ± 1.3	3.6 ± 0.7	–
NGC 4486	–	–	–	–	–
NGC 4589	–	0.3 ± 0.1	0.4 ± 0.1	–	–
NGC 4696	0.9 ± 0.1	4.9 ± 0.2	14.5 ± 0.5	4.0 ± 0.1	4.5 ± 0.2
NGC 4697	–	–	–	–	–
NGC 5011	–	3.1 ± 0.2	5.0 ± 0.2	–	–
NGC 5018	–	12.1 ± 2.7	18.3 ± 3.8	–	–
NGC 5044	1.5 ± 0.2	9.0 ± 0.3	44.4 ± 1.1	0.8 ± 0.1	1.4 ± 0.1
NGC 5077	2.6 ± 0.5	11.7 ± 0.6	45.6 ± 1.4	2.1 ± 0.5	1.6 ± 0.5
NGC 5090	0.8 ± 0.2	5.3 ± 0.4	12.9 ± 0.5	–	–
NGC 5813	–	–	–	–	–
NGC 7619	–	–	–	–	–
IC 1459	3.1 ± 1.0	23.5 ± 1.7	50.0 ± 2.2	–	–
IC 2006	–	–	–	–	–
IC 3370	0.7 ± 0.1	1.6 ± 0.2	0.9 ± 0.2	1.5 ± 0.2	–
IC 4296	–	10.1 ± 1.1	15.0 ± 0.8	2.0 ± 0.5	–
E/S0					
NGC 1052	–	84.6 ± 13.3	207.3 ± 18.4	–	–
NGC 4472	–	–	–	–	–
NGC 4550	–	–	–	–	–
NGC 4636	–	–	–	–	–
NGC 5353	0.8 ± 0.2	1.0 ± 0.3	3.4 ± 0.3	2.8 ± 0.4	2.9 ± 0.4
NGC 6868	–	22.3 ± 0.8	28.8 ± 1.0	2.8 ± 0.5	3.8 ± 0.5
S0					
NGC 584	–	–	–	–	–
NGC 1366	–	1.5 ± 0.1	2.7 ± 0.2	1.5 ± 0.2	–
NGC 1533	1.8 ± 0.3	6.3 ± 0.4	12.0 ± 0.4	0.5 ± 0.1	–
NGC 1553	–	15.4 ± 1.0	28.9 ± 1.8	–	7.5 ± 0.7
NGC 2685	1.7 ± 0.2	3.8 ± 0.3	12.9 ± 0.5	–	–
NGC 3245	–	–	–	–	–
NGC 4036	–	–	–	–	–
NGC 4371	–	–	–	–	–
NGC 4382	–	–	–	–	–
NGC 4383	–	459.9 ± 38.7	390.9 ± 26.8	–	–
NGC 4435	–	–	–	–	–
NGC 4477	–	16.8 ± 1.1	31.4 ± 1.5	–	–
NGC 4552	–	–	–	–	–
NGC 4649	–	–	–	–	–
NGC 5128		234.9 ± 77.3	–	–	–
NGC 5273	–	49.5 ± 4.1	83.2 ± 5.8	–	–
NGC 5631	1.7 ± 0.5	3.6 ± 0.2	9.4 ± 0.1	3.7 ± 0.3	–
NGC 5846	–	–	–	–	–
NGC 5898	–	4.5 ± 0.4	9.3 ± 0.5	–	2.0 ± 0.4
NGC 7192	–	2.7 ± 0.2	4.0 ± 0.2	–	–
NGC 7332	1.8 ± 0.3	4.7 ± 0.3	8.2 ± 0.7	1.0 ± 0.3	1.1 ± 0.2
IC 5063	–	480.5 ± 58.9	524.9 ± 66.5	–	–

Notes. Uncertainties are 1σ. Values are in units of 10^{-18} [W m^{-2}]. Neither atomic nor molecular emission lines are detected in passive ETGs. [d] The two lines are blended in LL1 spectra: the values reported are the result of a line de-blending.

Table B1. Optical activity class, nuclear X-ray luminosity and 1.4-GHz radio power.

Galaxy	RSA morph. type	Optical class	Log $L_{X, nuc}$ [erg s^{-1}]	$P_{1.4\,GHz}$ [W Hz^{-1}]	Galaxy	RSA morph. type	Optical class	Log $L_{X, nuc}$ [erg s^{-1}]	$P_{1.4\,GHz}$ [W Hz^{-1}]
NGC 636	E1	–	–	$<6.4 \times 10^{19}$	NGC 5090	E2	LIN(H)	–	–
NGC 720	E5	–	38.90	$<1.2 \times 10^{20}$	NGC 5638	E1	IN	–	$<4.1 \times 10^{19}$
NGC 821	E6	–	<38.37	$<6.3 \times 10^{19}$	NGC 5812	E0	IN	–	1.3×10^{20}
NGC 1209	E6	LIN(H)	–	1.9×10^{21}	NGC 5813	E1	LIN(W); L2:	38.80	1.8×10^{21}
NGC 1275	E pec	S1.5	–	1.4×10^{25}	NGC 5831	E4	IN	–	$<5.3 \times 10^{19}$
NGC 1297	E2	LIN(H)	–	$<5.9 \times 10^{19}$	NGC 7619	E3	–	40.84	6.8×10^{21}
NGC 1339	E4	–	–	$<4.2 \times 10^{19}$	IC 1459	E1	LIN(H)	40.87	1.3×10^{23}
NGC 1374	E0	–	–	$<2.3 \times 10^{19}$	IC 2006	E1	Comp(W)	–	4.9×10^{19}
NGC 1379	E0	–	–	$<1.4 \times 10^{19}$	IC 3370	E2 pec	LIN(H)	–	8.8×10^{20}
NGC 1395	E2	–	39.06	5.4×10^{19}	IC 4296	E0	LIN(H)	41.20	5.6×10^{24}
NGC 1399	E1		<38.96	1.2×10^{23}					
NGC 1404	E2	–	40.57	1.9×10^{20}	NGC 1052	E3/S0	LIN(H); L1.9	41.20	5.1×10^{22}
NGC 1407	E0	IN	<39.14	8.7×10^{21}	NGC 1351	S0$_1$/E6	–	–	4.9×10^{19}
NGC 1426	E4	IN	–	$<8.5 \times 10^{19}$	NGC 4472	E1/S0$_1$	S2::	<38.67	7.4×10^{21}
NGC 1427	E5	–	–	$<3.2 \times 10^{19}$	NGC 4550	E/S0	L2	<38.37	$<2.0 \times 10^{19}$
NGC 1453	E2	LIN(H)	–	9.5×10^{21}	NGC 4570	E7/S0$_1$	–	38.18	$<3.5 \times 10^{19}$
NGC 1549	E2	–	38.46	–	NGC 4636	E0/S0$_1$	LIN(H); L1.9	<38.24	2.0×10^{21}
NGC 1700	E3	–	38.84	$<3.3 \times 10^{20}$	NGC 5353	S0$_1$/E7	L2/T2	–	4.2×10^{21}
NGC 2300	E3	–	40.96	2.4×10^{20}	NGC 6868	E3/S0$_{2/3}$	LIN(H)	–	–
NGC 2974	E4	LIN(H)	40.32	5.7×10^{20}	NGC 584	S0$_1$	–	–	1.6×10^{21}
NGC 3193	E2	L2:	<39.74	$<1.1 \times 10^{20}$	NGC 1366	S0$_1$	IN	–	–
NGC 3258	E1	Comp(H)	–	6.2×10^{21}	NGC 1389	S0$_1$/SB0$_1$	IN	–	$<5.4 \times 10^{19}$
NGC 3268	E2	LIN(H)	–	3.7×10^{21}	NGC 1533	SB0$_2$/SBa	LIN(H)	–	–
NGC 3377	E6	–	38.24	$<1.8 \times 10^{19}$	NGC 1553	S0$_{1/2}$ pec	LIN(W)	40.22	–
NGC 3379	E0	L2/T2::	38.12	3.2×10^{19}	NGC 2685	S0$_3$ pec	S2/T2	–	3.3×10^{19}
NGC 3557	E3	LIN(W)	40.24	2.0×10^{23}	NGC 3245	S0$_1$	T2:	39.00	3.5×10^{20}
NGC 3608	E1	L2/S2:	38.21	8.2×10^{19}	NGC 4036	S0$_3$/Sa	L1.9	39.05	5.4×10^{20}
NGC 3818	E5	IN(Traces)	–	$<2.8 \times 10^{20}$	NGC 4339	S0$_{1/2}$	–	–	$<9.7 \times 10^{18}$
NGC 3904	E2	–	–	$<1.3 \times 10^{20}$	NGC 4371	SB0$_{2/3}$(r)	–	–	$<3.8 \times 10^{19}$
NGC 3962	E1	LIN(H)	–	3.4×10^{20}	NGC 4377	S0$_1$	–	–	6.0×10^{19}
NGC 4261	E3	L1	41.10	2.6×10^{24}	NGC 4382	S0$_1$ pec	–	–	$<6.1 \times 10^{19}$
NGC 4365	E3	–	38.25	$<3.2 \times 10^{19}$	NGC 4383	S0:	MRK star-form.	–	–
NGC 4374	E1	LIN(H); L2	39.50	2.9×10^{23}	NGC 4435	SB0$_1$	T2/H:; no AGN	38.45	–
NGC 4473	E5	–	<38.14	$<2.2 \times 10^{19}$	NGC 4442	SB0$_1$	–	–	$<1.4 \times 10^{19}$
NGC 4478	E2	–	<38.49	–	NGC 4474	S0$_1$	–	–	$<1.7 \times 10^{19}$
NGC 4486	E0	L2	40.80	6.9×10^{24}	NGC 4477	SB0$_{1/2}$/SBa	S2	–	$<7.4 \times 10^{19}$
NGC 4564	E6	–	38.45	4.9×10^{19}	NGC 4552	S0$_1$	Comp (W); T2:	39.20	3.1×10^{21}
NGC 4589	E2	L2	38.90	2.1×10^{21}	NGC 4649	S0$_1$	–	38.09	9.4×10^{20}
NGC 4621	E5	–	38.92	$<1.3 \times 10^{19}$	NGC 5128	S0+S pec	S2	41.88	4.4×10^{23}
NGC 4660	E5	–	38.22	$<3.5 \times 10^{19}$	NGC 5273	S0/a	S1.5	40.55	1.1×10^{20}
NGC 4696	E3	LIN(H)	40.00	–	NGC 5631	S0$_3$/Sa	S2/L2:	–	1.2×10^{20}
NGC 4697	E6	LIN(W)	38.41	5.2×10^{20}	NGC 5846	S0$_1$	LIN(H); T2	40.80	1.6×10^{21}
NGC 5011	E2	LIN(W)	–	–	NGC 5898	S0$_{2/3}$	LIN(W)	–	$<1.5 \times 10^{20}$
NGC 5018	E4	LLAGN	<39.41	3.5×10^{20}	NGC 7192	S0$_2$	LIN(W)	–	–
NGC 5044	E0	LIN(H)	39.44	4.0×10^{21}	NGC 7332	S0$_{2/3}$	IN(Traces)	<39.70	$<9.5 \times 10^{19}$
NGC 5077	E3	LIN(H); L1.9	–	2.8×10^{22}	IC 5063	S0$_3$/Sa	S2	–	–

The optical activity (columns 3 and 8) is derived from Annibali et al. (2010), who use the following notation: LlN, LINER; AGN, AGN-like emission; IN, either faint (traces) or no emission lines; Comp, transition between H II regions and LINERs. W and H indicate weak emission (EW(H$_\alpha$ +[N II]6584)$<$3 Å) and strong emission line galaxies, respectively. For the optical activity class, we also use the notation of Ho et al. (1997), namely S, Seyfert; L, LINERS; T, transition objects; H, H II region (: indicates uncertain estimates). The nuclear X-ray luminosity, $L_{X, nuc}$ (columns 4 and 9) and the radio power at 1.4 GHz, $P_{1.4\,GHz}$ (columns 5 and 10) are from Pellegrini (2010) and Brown et al. (2011), respectively.

4 and 9) and the radio power at 1.4 GHz (columns 5 and 10), which refers to the entire galaxy. In Tables B2 and B3 we report the kinematical and morphological peculiarities (columns 3 and 4) for Es and S0s, respectively. In column 5 we give the morphology of dust-lanes from optical observations. The kinematical peculiarities refer to the nuclear part of the galaxy, basically within one effective radius or less, so they provide a description of star and gas properties that contribute to the formation of the present *Spitzer*–IRS spectrum.

Table B2. Ellipticals: kinematical and morphological characterization from optical studies.

Galaxy	RSA morph. type	Gas versus stars kinematical peculiarities	Morphological peculiarities	Dust-lane morphology
NGC 636	E1	–	–	Asymmetric dust distribution (16)
NGC 720	E5	–	Boxy outer isophotes (6)	No dust (13)
NGC 821	E6	SC (4)	–	No dust (9)
NGC 1209	E6	–	X-like struct.; NW linear feature (6)	–
NGC 1297	E2	–	–	Dust-lane (a)
NGC 1275	E pec	–	Jet	Complex patches (18)
NGC 1339	E4	–	–	No dust (10)
NGC 1374	E0	–	–	No dust (10,11)
NGC 1379	E0	–	–	No dust (11)
NGC 1395	E2	–	NW perpend. feature (6); Low contr. shells (7)	–
NGC 1399	E1	–	–	No dust (10,11)
NGC 1404	E2	–	–	No dust (11)
NGC 1407	E0	Rotat. min. axis (a)	–	No dust (13)
NGC 1426	E4	–	–	No dust(10)
NGC 1427	E5	–	–	No dust (10,11)
NGC 1453	E2	g-d and g-maj t (a)	–	–
NGC 1549	E2	Stars rotat. min. axis (0)	Shells (7)	–
NGC 1700	E3	CR s-s(1)	–	Chaotic dust patches (10)
NGC 2300	E3	–	–	No-dust (10)
NGC 2974	E4	SC(4)	Multiple shells (6); g-d and g-maj t ≈20° (a)	Spiral dust-lanes (10)
NGC 3193	E2	–	–	No dust (9)
NGC 3258	E1	CR g-s (1)	–	No dust (13)
NGC 3268	E2	–	–	Small disc of dust (a,16)
NGC 3377	E6	Modest star rotat. min. axis (3); SC(4)	–	Chaotic dust patches and filam. (9,10)
NGC 3379	E0	SC (4)	–	Nuclear dust ring (10)
NGC 3557	E3	–	SW fan; asym. outer isophotes (6)	Nuclear ring of dust (10)
NGC 3608	E1	CR s-s (3); KDC (4)	–	Nuclear dust ring (10)
NGC 3818	E5	–	–	–
NGC 3904	E2	–	–	–
NGC 3962	E1	–	Gas disc+outer arc-like struct. (a)	Dust patches (a)
NGC 4261	E3	–	NW tidal arm/ faint SE fan (6)	Dust disc (9)
NGC 4365	E3	–	Faint SW fan (6)	No dust (10)
NGC 4374	E1	Rotat. vel. ≈0 (3); SC (4)	–	Dust-lane (a,9)
NGC 4473	E5	Complex morph. of σ and vel. field (3); MC (4)	–	No dust (10)
NGC 4478	E2	–	–	No dust (10)
NGC 4486	E0	V≈0 (3); SC(4)	Jet	No dust (9)
NGC 4589	E2	–	–	Chaotic dust patches (10)
NGC 4564	E6	SC (4)	–	No dust (9)
NGC 4621	E5	CR s-s inner 2 arcsec (3); KDC (4)	–	No dust (10)
NGC 4660	E5	Two disc components (3); MC (4)	–	No dust (9)
NGC 4696	E3	–	Faint outer shells (2)	Dust arc (a,11,13)
NGC 4697	E6	–	Non-spherical inner isophotes (6)	Disc (23)
NGC 5011	E2	–	–	No dust (11,13)
NGC 5018	E4	–	Multiple tidal tails and shells (6,7)	Dust nuclear ring/chaotic (10)
NGC 5044	E0	CR s-s; gas irr. motion (a)	Gas fil. shape (a)	Chaotic dust patches (15)
NGC 5077	E3	CR s-s (a); g-d and g-maj t ≈90° (a)	–	Dust filaments (9)
NGC 5090	E2	–	–	No dust (11,13)
NGC 5638	E1	–	–	–
NGC 5812	E0	–	Tidal tail (2)	Dust nuclear disc 0.4-arcsec diameter (a)
NGC 5813	E1	CR s-s; gas irr. motion (a); KDC (4)	Gas fil. shape (a)	Dust nuclear ring/chaotic (10)
NGC 5831	E4	CR s-s (2,3); KDC (4)	–	No dust (9)
NGC 7619	E3	Rotat. min. axis (17)	–	No dust (10)
IC 1459	E1	CR g-g (1)	Multiple shells (6)	Dust nuclear ring/chaotic (10)
IC 2006	E1	CR g-s (1)	–	–
IC 3370	E2 pec	–	X-like struct.; broad N fan (6); polar ring? (5)	Spiral dust-lane (10,11)
IC 4296	E0	CR s-s (a)	–	Nuclear ring (10)

In column 3 we use the following notation: CR g-s, counter-rotation gas versus stars; CR s-s, counter-rotation stars versus stars; CR g-g, counter-rotation gas versus gas; Rotat. min. axis, stars rotate along the galaxy minor axis; g-d and g-maj t, gas disc and galaxy major axis are tilted by the reported angle, if provided in the literature. KDC, kinematical decoupled component, not necessarily counter-rotation; MC, multiple components; SC, single component (see Krajnović et al. 2008). A description of the kinematical and morphological peculiarities of the galaxies and full references are reported in Rampazzo et al. (2005) and Annibali et al. (2006), labelled by (a). Further kinematical references: (0) Rampazzo (1988); (1) Corsini et al. (1998); (2) Davies et al. (1983); (3) Emsellem et al. (2004); (4) Krajnović et al. (2008); (5) Sil'chenko, Moiseev & Afanasiev (2009). Morphological peculiarities are from: (6) Tal et al. (2009); (7) Malin & Carter (1983); (8) Pierfederici & Rampazzo (2004). The dust detection and structure in the optical bands are from (9) Zhang, Gu & Ho (2008); (10) Lauer et al. (2005); (11) Sadler & Gerhard (1995); (12) Coccato et al. (2004); (13) Véron-Cetty & Véron (1988); (14) Morganti et al. (2007); (15) Temi, Brighenti & Mathews (2007); (16) Ferrari et al. (2002); (17) Pu et al. (2010); (18) Tremblay et al. (2007); (19) Wiklind & Henkel (2001); (20) Simões et al. (2007); (21) Pinkney et al. (2003); (22) Patil et al. (2007); (23) van Dokkum & Franx (1995); (24) Kormendy et al. (2009); Whitmore et al. (1990).

Table B3. E/S0s and S0s: kinematical and morphological characterization from optical studies.

Galaxy	RSA morph. type	Gas versus stars kinematical peculiarities	Morphological peculiarities	Dust-lane morphology
NGC 1052	E3/S0	CR g-g (1,a)	–	Dust (9)
NGC 1351	$S0_1$/E6	–	–	No dust (11)
NGC 4472	E1/$S0_1$	CR s-s (1)	–	Chaotic dust patches (10)
NGC 4550	E/S0	CR -ss (1); slow rot. (3); SC (4)	–	Asymmetric dust patches (19)
NGC 4570	E7/$S0_1$	MC (4)	–	No dust (20)
NGC 4636	E0/S01(6)	Gas irr. motion (a)	–	Dust-lanes (9)
NGC 5353	$S0_1$/E7	–	–	–
NGC 6868	E3/S02/3(3)	CR g-s (a)	–	Dust patches (a,11)
NGC 584	$S0_1$	–	Non-spherical isophotes (6)	Chaotic dust patches (10)
NGC 1366	E7/S01(7)	–	–	–
NGC 1389	S01(5)/SB01	–	–	No dust (11)
NGC 1533	SB02(2)/SBa	–	–	No dust (11)
NGC 1553	S01/2(5)pec	–	Shells (7)	No dust (13)
NGC 2685	$S0_3$ pec	σ double peak (7); SC (4) gas min. axis grad (12)	Polar ring (25)	Polar dust lanes (7)
NGC 3245	$S0_1$	–	–	–
NGC 4036	$S0_3$/Sa	Gas min. axis grad (12)	–	Irr. dust structures (20)
NGC 4339	$S0_{1/2}$	–	–	–
NGC 4371	$SB0_{2/3}$(r)	–	–	Dust disc (20)
NGC 4377	$S0_1$	–	–	–
NGC 4382	$S0_1$ pec	CR s-s (3); MC(4)	Shells (24)	No dust (10) or weak (20)
NGC 4383	S0:	Gas min. axis grad (12)	–	–
NGC 4435	$SB0_1$	–	Interact. with NGC 4438	Dust nuclear disc (12)
NGC 4442	$SB0_1$	–	–	–
NGC 4474	$S0_1$	–	–	–
NGC 4477	$SB0_{1/2}$/SBa	CR s-s (1); SC (4)	Kin. and phot. axes misaligned (3)	Dust spiral (20)
NGC 4552	S01(0)	KDC (4)	Shells (7)	Chaotic dust patches (10)
NGC 4649	$S0_1$	Asym. rot. curve (21)	–	No dust (10)
NGC 5128	S0+S pec	Gas min. axis grad (12)	Many shells (7), warps (11)	Strong dust lane (11)
NGC 5273	S0/a	–	–	Weak dust features (20)
NGC 5631	$S0_3$/Sa	CR (g-s) (5)	–	–
NGC 5846	$S0_1$(0)	Gas irr. motion (a); SC(4)	Faint outer shells (6)	Dust filaments extended (a)
NGC 5898	$S0_{2/3}$(0)	CR g-s (1); Gas min. axis grad (12)	Three spiral arm-like tidal tails (6)	Dust patches (22)
NGC 7192	$S0_2$(0)	CR s-s (a)	Shell (6)	No dust (13)
NGC 7332	$S0_{2/3}$	CR g-g (1); KDC (4); gas min. axis grad (12)	–	–
IC 5063	$S0_3$(3)pec/Sa	Gas min. axis grad (12)	–	Dust-lane (14)

References and legends as in Table B2.

This paper has been typeset from a TEX/LATEX file prepared by the author.